

# Electron-Capture Supernova Candidates from Light Curves: Implications for Their Progenitors and Explosion Properties

MASATO SATO <sup>1</sup>, NOZOMU TOMINAGA <sup>2,3,4</sup>, SERGEI I. BLINNIKOV <sup>5,6</sup>, MARAT SH. POTASHOV <sup>5,6,7</sup>,  
TAKASHI J. MORIYA <sup>2,3,8</sup>, DAICHI HIRAMATSU <sup>9</sup>, FRANCISCO FÖRSTER <sup>10,11,12</sup> AND JOSEPH P ANDERSON <sup>13</sup>

<sup>1</sup>Department of Earth Science and Astronomy, The University of Tokyo, 3-8-1 Komaba, Meguro-ku, Tokyo 153-8902, Japan

<sup>2</sup>National Astronomical Observatory of Japan, National Institutes of Natural Sciences, 2-21-1 Osawa, Mitaka, Tokyo 181-8588, Japan

<sup>3</sup>Astronomical Science Program, Graduate Institute for Advanced Studies, SOKENDAI, 2-21-1 Osawa, Mitaka, Tokyo 181-8588, Japan

<sup>4</sup>Department of Physics, Faculty of Science and Engineering, Konan University, 8-9-1 Okamoto, Kobe, Hyogo 658-8501, Japan

<sup>5</sup>NRC Kurchatov Institute, 123182 Moscow, Russia

<sup>6</sup>Sternberg Astronomical Institute, MSU, 119234 Moscow, Russia

<sup>7</sup>Keldysh Institute of Applied Mathematics RAS, 4 Miusskaya Square, 125047 Moscow, Russia

<sup>8</sup>School of Physics and Astronomy, Monash University, Clayton, Victoria 3800, Australia

<sup>9</sup>Department of Astronomy, University of Florida, 211 Bryant Space Science Center, Gainesville, FL 32611-2055, USA

<sup>10</sup>Data and Artificial Intelligence Initiative (IDIA), Faculty of Physical and Mathematical Sciences, Universidad de Chile, Santiago, Chile

<sup>11</sup>Millennium Institute of Astrophysics, Nuncio Monseñor Sotero Sanz 100, Of. 104, Providencia, Santiago, Chile

<sup>12</sup>Center for Mathematical Modeling, Universidad de Chile, Beauchef 851, Santiago 8370456, Chile

<sup>13</sup>European Southern Observatory, Alonso de Córdova 3107, Vitacura, Casilla 19001, Santiago, Chile

## ABSTRACT

Core-collapse supernovae are explosions of massive stars. While most massive stars end as iron-core-collapse supernovae, less massive stars are expected to explode as electron-capture supernovae (ECSNe), defining the low-mass boundary of core-collapse supernovae. ECSNe were proposed  $\sim 40$  years ago, and first-principles simulations predict their successful explosions with low energies of  $\sim 10^{50}$  erg. Nevertheless, only one convincing candidate, SN 2018zd, has been proposed other than SN 1054, the progenitor of the Crab Nebula. We search for ECSN candidates among Type II SNe from the literature and a public Zwicky Transient Facility sample, using a color-based diagnostic, selecting ten candidates with blue colors at the middle of the plateau. We classify three as *gold*, for which a spectrum around the middle of the plateau disfavors strong circumstellar-medium interaction that would make the SN bluer, and seven as *silver* without such spectra. Comparing the observed multicolor light curves with radiation-hydrodynamical models, we infer the explosion energies,  $(0.4-1.7) \times 10^{50}$  erg for the *gold candidates* and  $(0.4-2.7) \times 10^{50}$  erg including the *silver candidates*, consistent with first-principles predictions and the mass-loss rates,  $3 \times 10^{-3} - 3 \times 10^{-2} M_{\odot} \text{ yr}^{-1}$  for the *gold candidates*, which remain similar when the *silver candidates* are included, higher than those expected for the early super-asymptotic-giant-branch phase. The ECSN occurrence ratios among SNe II are inferred as  $3.0^{+10.6}_{-2.9}$  and  $15.7^{+17.3}_{-12.7}$  % from the *gold* and *silver candidates*, respectively, which we interpret as lower and upper limits. To robustly identify ECSNe and refine this ratio, spectroscopic follow-ups of ECSN candidates around the middle of the plateau are essential.

**Keywords:** Type II supernovae (1731) — Stellar evolution (1599) — Stellar astronomy (1583) — Photometry (1234)

## 1. INTRODUCTION

Core-collapse supernovae (CCSNe) are the terminal explosions of massive stars, triggered by the collapse of

their cores. Collapsing cores are divided into two mass-dependent types: Iron (Fe) cores, for which progenitors are massive enough to ignite static Si burning, collapse because of photo-disintegration and the stars explode as Fe-core-collapse supernovae (FeCCSNe, S. A. Colgate & R. H. White 1966; H. A. Bethe 1985; S. E. Woosley et al. 2002). Oxygen-neon-magnesium (ONeMg) cores,

for which progenitors are not massive enough to ignite Ne burning, are supported by electron degeneracy pressure. Degenerate ONeMg cores collapse owing to electron capture by Mg and Ne, and the stars explode as electron-capture supernovae (ECSNe, [S. Miyaji et al. 1980](#); [K. Nomoto et al. 1982](#); [K. Nomoto 1984, 1987](#)). The progenitors of ECSNe are likely to be less massive than those of FeCCSNe, defining the low-mass end of the CCSN-progenitor distribution.

The progenitors of ECSNe are super-asymptotic-giant-branch (super-AGB) stars if they retain a hydrogen-rich (H-rich) envelope. The terminal fate of a super-AGB star is governed by the competition between mass loss from the envelope and the growth of its degenerate core ([L. Siess 2007](#); [C. L. Doherty et al. 2017](#); [M. Limongi et al. 2024](#)). If the mass loss dominates, the envelope is completely stripped before the core reaches the Chandrasekhar mass, leaving an ONe white dwarf. If the core growth proceeds faster, the core mass approaches to the Chandrasekhar limit and collapses via electron captures, leading to an ECSN. Recent stellar-evolution models suggest that the mass-loss rate during the early super-AGB phase is around  $10^{-5}$ – $10^{-4} M_{\odot} \text{ yr}^{-1}$  ([M. Limongi et al. 2024](#)), but how this rate evolves toward the end of the super-AGB phase and whether episodic enhancements of mass loss occur remain uncertain. If both the mass-loss and core-growth rates are sustained, the estimate of lower-mass limit for a star to explode as an ECSN is  $8.50 M_{\odot}$  ([M. Limongi et al. 2024](#)). Combined with the estimate of the upper-mass limit of  $9.22 M_{\odot}$  – the minimum mass for a star to ignite Ne burning – this implies that ECSNe could account for  $\sim 10\%$  of all CCSNe, assuming a standard initial mass function ([E. E. Salpeter 1955](#)). However, some studies suggest that the stellar mass window for ECSNe may be non-existent for solar metallicity ([N. Langer 2012](#)) because of a strong metal-driven mass loss. Consequently, the initial mass range for ECSNe remains highly uncertain and likely depends sensitively on metallicity.

ECSN explosions have been successfully simulated under the assumption of spherical symmetry owing to the low-density envelopes of their progenitors ([F. S. Kitaura et al. 2006](#)) in contrast to FeCCSNe for which multi-dimensional effects such as convection and turbulence are crucial for successful explosions ([T. Takiwaki et al. 2012](#)). First-principles simulations revealed a low explosion energy,  $\sim 10^{50}$  erg, and small amount of  $^{56}\text{Ni}$ ,  $0.002$ – $0.004 M_{\odot}$ , for ECSNe ([F. S. Kitaura et al. 2006](#); [H.-T. Janka et al. 2008](#); [S. Wanajo et al. 2009](#)). The elemental abundance ratios are consistent with the Crab Nebula, a remnant of SN 1054 ([K. Davidson et al. 1982](#);

[K. Nomoto et al. 1982](#); [S. Wanajo et al. 2009](#); [T. Temim et al. 2024](#)).

ECSNe are observed as H-rich Type II supernovae (SNe II)<sup>14</sup> if the progenitors retain a H-rich envelope, similarly to FeCCSNe from H-rich red-supergiant (RSG) progenitors ([N. Tominaga et al. 2013](#); [T. J. Moriya et al. 2014](#)). When an SN II occurs in the absence of a dense circumstellar medium (CSM), the SN exhibits an initial shock-breakout flash. After the shock breakout, a plateau phase follows, powered by the release of energy from the shock-heated H-rich envelope. The duration and luminosity of the plateau reflect the explosion energy, pre-supernova radius, and envelope mass of the progenitor ([I. Y. Litvinova & D. K. Nadezhin 1985](#); [D. V. Popov 1993](#); [R. G. Eastman et al. 1994](#); [D. Kasen & S. E. Woosley 2009](#)). The subsequent tail phase is generally powered by the radioactive decay of  $^{56}\text{Co}$ , the daughter nucleus of  $^{56}\text{Ni}$  synthesized during explosive nucleosynthesis, and its luminosity is approximately proportional to the ejected  $^{56}\text{Ni}$  mass. If the explosion occurs within a dense CSM, an early blue brightening – so-called wind breakout – is observed instead of the canonical shock breakout, as the breakout radiation diffuses through the CSM ([R. A. Chevalier & C. M. Irwin 2011](#); [T. Moriya et al. 2011](#); [V. Morozova et al. 2017](#); [T. J. Moriya et al. 2018](#)). Moreover, depending on the extent of the CSM, ejecta-CSM interaction can further contribute to the luminosity by efficiently converting kinetic energy into radiation, from early times to the tail phase.

The bolometric light curves of ECSNe exhibit plateaus of  $-15$  to  $-16$  mag ([N. Tominaga et al. 2013](#)), similarly to those of H-rich FeCCSNe with  $\sim -15$  to  $-18$  mag ([T. Sukhbold et al. 2016](#)), despite their low explosion energies, owing to the extended progenitor envelope structure. By contrast, the tails of ECSNe are faint,  $\sim -11$  mag at the onset, due to the low  $^{56}\text{Ni}$  yields, resulting in a large drop of  $\sim 4$  mag from plateau to tail whereas FeCCSNe exhibit tails of  $\sim -12.5$  to  $-15.5$  mag at the onset, and a drop of  $\sim 2.5$  mag from plateau to tail. ECSNe also display distinctly bluer plateau colors than low-mass FeCCSNe without significant CSM interaction, reflecting the low-density and extended envelope structure of super-AGB progenitors due to their degenerate cores ([A. Kozyreva et al. 2021](#); [M. Sato et al. 2024](#)). Leveraging this blue-plateau signature, [M. Sato et al. \(2024\)](#) proposed a new color-based diagnostic to discriminate ECSNe from low-mass FeCCSNe.

SNe II have been extensively discovered and investigated by modern transient surveys and follow-up pro-

<sup>14</sup> In this paper, “SNe II” does not include Type IIn or I Ib SNe.

grams, such as the Zwicky Transient Facility (ZTF, [E. C. Bellm et al. 2018](#)). The upcoming Vera C. Rubin Observatory’s Legacy Survey of Space and Time (LSST; [LSST Science Collaboration et al. 2009](#)) is expected to further accelerate such discoveries. From the Lick Observatory Supernova Search (LOSS, [J. Leaman et al. 2011](#); [W. Li et al. 2011a](#)) survey, the volumetric CCSN rate was estimated as  $(7.1 \pm 1.1) \times 10^4 \text{ Gpc}^{-3} \text{ yr}^{-1}$ , with SNe II comprising about 58% of all CCSNe ([W. Li et al. 2011b](#)), broadly consistent with other surveys ([K. K. Das et al. 2025a](#); [T. Pessi et al. 2025](#)).

Despite the robust explosion prediction in first-principles simulations and the extensive survey of SNe II, observations of ECSNe have remained elusive. Recently, [D. Hiramatsu et al. \(2021\)](#) proposed SN 2018zd as a promising ECSN candidate on the basis of several observational features and indications which are consistent with theoretical expectations, i.e., light-curve morphology, low explosion energy, the presence of dense CSM, nucleosynthetic yields, and progenitor identification (see also [S. D. Van Dyk et al. 2022](#)). A complementary search within the ZTF Census of the Local Universe (ZTF-CLU; [K. De et al. 2020](#)) program, a galaxy-targeted, volume-limited effort that aims for spectroscopic completeness of ZTF transients to a magnitude less than 20 mag within  $100''$  of CLU galaxies ([D. O. Cook et al. 2019](#)) out to  $\sim 200$  Mpc, found no secure new ECSN candidates using the color-based diagnostic ([K. K. Das et al. 2025b](#)). These studies motivate a broader, systematic exploration to observationally constrain the occurrence rate, progenitor properties, and explosion physics of ECSNe.

Here, we undertake a broad search for ECSN candidates among previously reported SNe II in the literature and among ZTF public results, using our color-based diagnostic. Using our candidates, we infer a volumetric occurrence rate of ECSNe. We also compare the observed multicolor light curves with radiation-hydrodynamical models to infer explosion and progenitor properties.

This paper is structured as follows. Section 2 introduces the SN II sample, their observational quantities, and the selection method of ECSN candidates. Section 3 describes the light-curve models and methods to compare the models with observations. Section 4 presents the selection of ECSN candidates, their observational properties, and comparisons to theoretical light-curve models. Section 5 discusses the progenitor and explosion properties implied by the comparison to models as well as the inferred occurrence rate of ECSNe. Section 6 provides a summary of the main results and future prospects.

## 2. SAMPLE

### 2.1. SN II sample compilation

We compile two complementary samples of SNe II. The first is a literature sample having dense multi-band photometric data obtained by prior compilation studies ([T. Faran et al. 2014](#); [S. Valenti et al. 2016](#); [L. Galbany et al. 2016](#); [J. P. Anderson et al. 2024](#)) with selected individual SNe of particular relevance, the promising ECSN candidate, SN 2018zd ([D. Hiramatsu et al. 2021](#)), an SN II with a blue color plateau, SN 2023axu ([M. Shrestha et al. 2024](#)), and the prototypical low-luminosity SN 2005cs ([A. Pastorello et al. 2009](#)). The SNe II from [A. Pastorello et al. \(2009\)](#); [T. Faran et al. \(2014\)](#); [S. Valenti et al. \(2016\)](#); [D. Hiramatsu et al. \(2021\)](#); [M. Shrestha et al. \(2024\)](#) are corrected for both Milky-Way and host-galaxy extinctions, whereas those from [L. Galbany et al. \(2016\)](#); [J. P. Anderson et al. \(2024\)](#) are corrected only for the Milky-Way extinction. While host-galaxy extinction is not negligible for some SNe II (e.g., [D. C. Leonard et al. 2002](#)), it does not appear to dominate the observed color diversity of SNe II and may be modest in many cases ([T. de Jaeger et al. 2018](#); [K. K. Das et al. 2025a](#)). These SNe II are observed in some or all of the filters of  $g$ ,  $r$ , and  $i$  bands of Sloan Digital Sky Survey system (SDSS, [M. Fukugita et al. 1996](#)),  $U$ ,  $B$ , and  $V$  bands of Johnson-Cousins system ([M. S. Bessell 2005](#)),  $UVW2$ ,  $UVM1$ ,  $UVW1$ ,  $U$ ,  $B$ , and  $V$  bands of Swift UltraViolet and Optical Telescope (UVOT, [T. S. Poole et al. 2007](#)) and unfiltered observations of T. Noguchi. We adopt the literature value for the explosion epoch,  $t_{\text{exp}}$ , and set  $t_{\text{exp}}$  as the origin of time through this paper.

From the SNe II obtained from the literature, we discard those having a larger gap than 10 days between the  $t_{\text{exp}}$  and the first detection to select SNe II with well-constrained  $t_{\text{exp}}$  estimation. Next we discard the objects that are not observed by the end of the plateau,  $t_{\text{end}}$ . We derive  $t_{\text{end}}$  following [J. P. Anderson et al. \(2014\)](#) as the epoch at which the object gets 0.1 mag fainter than the extrapolation of the straight line of the light-curve plateau. We then discard the objects that do not show a light-curve plateau by visual inspection and finally obtain 36 SNe II from the literature.

The second is the ZTF survey sample ([E. C. Bellm et al. 2018](#); [F. J. Masci et al. 2019](#)), which offers a systematic sample, enabling an estimate of the volumetric rate although the observation is limited to  $g$ ,  $r$ , and  $i$  bands of ZTF system. We follow a similar way to [J. Silva-Farfán et al. \(2024\)](#) to select SNe II observed by ZTF. We first adopt the Automatic Learning for the Rapid Classification of Events (ALeRCE) broker light-

curve classifier (F. Förster et al. 2021; P. Sánchez-Sáez et al. 2021) to select all the objects discovered before 2024-12-31 and classified as an SN II with a probability higher than 0.4. Then, we compare them with the Transient Name Server (TNS) database and select 683 objects that are spectroscopically classified as SNe II.

We obtain forced-photometry data from the ZTF forced-photometry service (F. J. Masci et al. 2019) for all SNe II. We first supply the coordinates of the SNe II from the TNS database and the time range from a sufficiently earlier (greater than 50 days) epoch to a sufficiently later (greater than 400 days) epoch than the first detection to obtain better baseline. Then, we subtract the baseline from the differential-flux measurements, rescale the flux uncertainties using the PSF-fit reduced- $\chi^2$  and the scatter of the baseline S/N, and obtain apparent-magnitude forced-photometry light curves, following F. J. Masci et al. (2019), with  $3\sigma$  detections, i.e.,  $S/N > 3$ , and  $5\sigma$  upper limits for non-detections.

To produce absolute-magnitude light curves, we adopt redshifts from the TNS database and a standard  $\Lambda$ CDM model with the Hubble constant,  $H_0 = 70.4 \text{ km Mpc}^{-1} \text{ s}^{-1}$  and the density parameter,  $\Omega_0 = 0.272$  (E. Komatsu et al. 2011). We also correct for dust extinction, adopting the Milky-Way extinction (D. J. Schlegel et al. 1998) at a coordinate where the forced photometry is obtained and assuming  $R_V = 3.1$ . We do not correct for the host-galaxy extinction similarly to the literature SNe II from L. Galbany et al. (2016); J. P. Anderson et al. (2024).

We consider the middle point between the last non-detection and earlier of the first detection and discovery as  $t_{\text{exp}}$  for the SNe II obtained from ZTF. We then discard the objects that have a gap greater than 10 days between each observation, including the non-detection. Next we discard the objects that are not observed by the end of the plateau in the same way as done for the literature sample and finally obtain 62 SNe II from the ZTF survey, named the ZTF survey sample. Integrating the literature and ZTF survey samples, we finally obtain 98 SNe II in total.

We next derive  $t_{\text{PT}}$ , the mid-point of the plateau end and tail onset, and the color index  $g - r$  or  $B - V$  at  $t_{\text{PT}}/2$ ,  $(g - r)_{t_{\text{PT}}/2}$  or  $(B - V)_{t_{\text{PT}}/2}$ . We adopt  $t_{\text{PT}}$  from literature if available. Otherwise, we estimate  $t_{\text{PT}}$  following the same method as O. E. Felipe et al. (2010); J. P. Anderson et al. (2014), except that we adopt the  $r$  band in the case  $V$  band is unavailable. With the  $t_{\text{PT}}$ , we derive  $(g - r)_{t_{\text{PT}}/2}$  and/or  $(B - V)_{t_{\text{PT}}/2}$ , depending on the available photometry, linearly interpolating the light curves in the corresponding band. The  $t_{\text{exp}}$ ,  $t_{\text{PT}}$ ,  $(g - r)_{t_{\text{PT}}/2}$ , and  $(B - V)_{t_{\text{PT}}/2}$  of the SNe II are listed in

Table 3 in Appendix A with the reference from which we obtain the photometry data. Figure 1 shows an example of the derived  $t_{\text{exp}}$ ,  $t_{\text{end}}$ ,  $t_{\text{PT}}$ , and  $t_{\text{PT}}/2$  for a ZTF survey sample object, SN 2022jps, along with its  $r$ -band light curve.

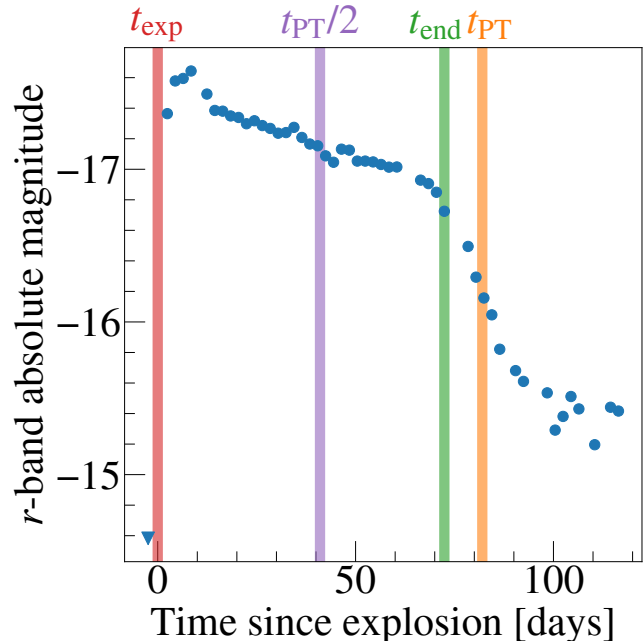


**Figure 1.** Example  $r$ -band light curve of a ZTF survey sample object, SN 2022jps. The blue circles indicate the detections after 1-day binning for visual clarity and the blue downward triangle indicates the last non-detection. The derived  $t_{\text{exp}}$ ,  $t_{\text{PT}}/2$ ,  $t_{\text{end}}$ , and  $t_{\text{PT}}$  are also indicated by the vertical red, purple, green, and orange lines, respectively. We set  $t_{\text{exp}}$  as the origin of time in this work.  $t_{\text{PT}}/2$  is the middle point between  $t_{\text{exp}}$  and  $t_{\text{PT}}$ , at which the color diagnostic is evaluated.

## 2.2. Selection of ECSN candidates

We adopt the color-based ECSN diagnostic method proposed by M. Sato et al. (2024). Performing one-dimensional radiation-hydrodynamical light-curve calculations for 736 ECSN and 1266 low-mass FeCCSN models spanning a wide range of physical parameters (e.g., explosion energy and CSM density profile), they show that the ECSNe exhibit systematically bluer plateaus than the FeCCSNe in the absence of strong CSM interaction, reflecting the low-density, extended hydrogen-rich envelopes of the ECSN progenitors, which place the photosphere deeper than the H-recombination front during the plateau. They also show that, for a given  $t_{\text{PT}}$ , the ECSNe have bluer color indices at  $t_{\text{PT}}/2$  than the FeCCSNe in the absence of strong CSM interaction at  $t_{\text{PT}}/2$ , and propose empirical linear boundaries

that separate the ECSNe and the FeCCSNe as an ECSN diagnostic. Specifically, ECSNe are expected to satisfy

$$(g - r)_{t_{\text{PT}}/2} < 0.008 \times t_{\text{PT}} - 0.4 \quad (1)$$

or

$$(B - V)_{t_{\text{PT}}/2} < 0.0089 \times t_{\text{PT}} - 0.36. \quad (2)$$

which correspond to Equations (3) and (C1) of [M. Sato et al. \(2024\)](#), respectively. Considering the uncertainties in the photometry and its analysis (e.g., extinction corrections), we select photometric ECSN candidates as events that satisfy either the  $g-r$  criterion (Equation 1) or the  $B-V$  criterion (Equation 2), using the available color information.

This diagnostic effectively separates ECSN and low-mass FeCCSN models and successfully identified SN 2018zd as an ECSN candidate. We note that the method assumes the absence of strong CSM interaction at  $t_{\text{PT}}/2$ , as an FeCCSN can also be blue in the presence of a strong CSM interaction. Therefore, when available, we assess the presence or absence of strong CSM interaction using spectra obtained around  $t_{\text{PT}}/2$ , in practice within about  $\pm 10$  days, focusing in particular on narrow lines, whose presence indicates the presence of dense CSM ([O. Yaron et al. 2017](#); [R. J. Bruch et al. 2021, 2023](#)). Although CSM interaction enhances the luminosity as well, it is difficult to discern it from the intrinsic SN luminosity or from enhancements due to other mechanisms. We therefore rely solely on spectroscopic, rather than photometric, properties to exclude SNe that interact with a dense CSM from ECSN candidates.

For the selected ECSN candidates, we adopt  $M(^{56}\text{Ni})$  inferred from the tail luminosity. Tail-based  $M(^{56}\text{Ni})$  estimates are typically obtained by converting a pseudo-bolometric luminosity to  $M(^{56}\text{Ni})$  assuming full deposition of the radioactive decay power ([W. D. Arnett 1980](#); [D. K. Nadyozhin 1994](#)), or scaling a pseudo-bolometric tail luminosity to that of SN 1987A evaluated over a comparable filter set ([S. Spiro et al. 2014](#)). We adopt the latter approach similarly to that adopted for SN 2018zd by [D. Hiramatsu et al. \(2021\)](#). We compute pseudo-bolometric luminosity following [S. Valenti et al. \(2007\)](#) using multi-band photometry between  $t_{\text{PT}} + 15$  and  $t_{\text{PT}} + 60$  days since explosion, and calculate  $M(^{56}\text{Ni})$  following [S. Spiro et al. \(2014\)](#). When late-time band coverage is insufficient, we derive an upper limit on  $M(^{56}\text{Ni})$  using the available photometric upper limits. Since the ejecta masses of ECSNe are lower than that of SN 1987A ( $\sim 14 M_{\odot}$ ; [T. Shigeyama & K. Nomoto 1990](#)), the  $\gamma$ -ray optical depths of ECSNe may be lower than that of SN 1987A, possibly resulting in an underestimate of  $M(^{56}\text{Ni})$ . However, since  $\gamma$ -rays are expected

to be almost fully deposited in the early tail phase, the difference in the ejecta mass does not significantly affect the  $M(^{56}\text{Ni})$  estimates. Note that the tail may also be powered by CSM interaction ([T. J. Moriya et al. 2014](#)) and/or pulsar spin-down ([N. Tominaga et al. 2013](#)). In that case, the true  $M(^{56}\text{Ni})$  may be lower than the values inferred from the tail luminosity.

We also derive  $\text{H}\alpha$  and  $\text{Fe II } \lambda 5169$  line velocity,  $v_{\text{H}\alpha}$  and  $v_{\text{Fe II}}$ , of ECSN candidates from their optical spectral sequences if available. We measure these velocities from the blue-shifted absorption trough of the P-Cygni profile, after correcting for redshift and extinction and subtracting the continuum.

### 3. MODEL

We adopt a two-step approach to model the observed multicolor light curves of ECSN candidates. Step 1 explores a broad parameter space with theoretically expected  $M(^{56}\text{Ni})$  and identifies a set of top-ranked models (i.e., those with lower  $\chi^2$ ) for each candidate. Step 2 refines the search with a denser local exploration around the top-ranked region from Step 1, setting  $M(^{56}\text{Ni})$  to the tail-based estimates (Section 2.2), and the best-fitting model is simply taken as the one with the lowest  $\chi^2$ . For both steps, we calculate  $\chi^2$  by simply summing residuals over all bands and epochs between  $t_{\text{exp}}$  and  $t_{\text{PT}}$  because modeling multicolor light curves in the tail phase requires solving the balance between radioactive heating and numerous line cooling, which is beyond the scope of this study. Although we do not include the tail phase in the  $\chi^2$  calculation, we adjust  $M(^{56}\text{Ni})$  because radioactive heating extends the plateau ([D. Kasen & S. E. Woosley 2009](#); [A. Kozyreva et al. 2019](#)).

#### 3.1. Progenitors

We adopt the super-AGB progenitor models from [N. Tominaga et al. \(2013\)](#) to calculate ECSN light curves. The hydrostatic and thermal equilibrium envelopes are attached to the  $1.377 M_{\odot}$  ONeMg cores of [K. Nomoto et al. \(1982\)](#); [K. Nomoto \(1984, 1987\)](#). Since super-AGB stars experience uncertain mass loss and third dredge-up from thermal pulses, we consider various envelope masses  $M_{\text{env}}$  and H abundances in the envelope  $X(\text{H})_{\text{env}}$ .

We adopt the nucleosynthesis yields from [S. Wanajo et al. \(2009\)](#). We adopt an inner mass cut at  $1.363 - 1.373 M_{\odot}$  to reduce the calculation cost, although it is estimated as  $1.362 M_{\odot}$  in the first-principles simulation ([F. S. Kitaura et al. 2006](#)). This small difference does not substantially affect the light curve properties, especially on the plateau phase.

While the first-principles simulations ([F. S. Kitaura et al. 2006](#); [H.-T. Janka et al. 2008](#)) predict the explo-

sion energy of an ECSN as  $E_{\text{exp}} \sim 10^{50}$  erg, we explore a wider range to account for possible diversity among candidates.

On top of the progenitor models, we attach a CSM structure following T. J. Moriya et al. (2018), with density

$$\rho_{\text{CSM}}(r) = \frac{\dot{M}}{(4\pi v_{\text{wind}})r^2}, \quad (3)$$

up to  $r = r_{\text{out}}$ , where  $r$  is the distance from the center of the star,  $v_{\text{wind}}$  is the wind velocity, and  $r_{\text{out}}$  is the CSM radius though the mechanism driving the wind is yet to be revealed. For the wind velocity, acceleration was considered using a simple  $\beta$  velocity law:

$$v_{\text{wind}}(r) = v_0 + (v_{\infty} - v_0) \left(1 - \frac{R}{r}\right)^{\beta}, \quad (4)$$

where  $v_0$  is the initial velocity of the wind,  $v_{\infty}$  is the terminal velocity of the wind, and  $R$  is the progenitor radius. Since the mass loss of super-AGB stars just before the explosion is uncertain, we consider wide parameter ranges for the CSM profile as listed in table 1.

In Step 1, we explore a broad parameter space as listed in Table 1. In total, we consider 2080 models in Step 1.

In Step 2, we perform a local refinement around the top-ranked region from Step 1 and set  $M(^{56}\text{Ni})$  to the tail-based estimate (Section 2.2). We placed  $^{56}\text{Ni}$  at the bottom of the ejecta. We do not consider the  $^{56}\text{Ni}$  mixing because 3D simulations of ECSN explosions predict small mixing (G. Stockinger et al. 2020) and it has little impact on plateau duration and luminosity (E. Nakar et al. 2016; T. J. Moriya et al. 2015; A. Kozyreva et al. 2019).

### 3.2. Light-curve Calculations

We adopt the one-dimensional multi-group radiation hydrodynamics code STELLA to calculate light curves because it solves radiation hydrodynamics with non-equilibrium prescription between gas and radiation (S. I. Blinnikov & O. S. Bartunov 1993; S. I. Blinnikov et al. 1998; S. Blinnikov et al. 2000), which is required in the low-density regions, i.e., the super-AGB envelope and CSM. STELLA first injects thermal energy at the center of the progenitor and solves time-dependent equations about the angular moments of averaged intensity over up to 100 fixed-frequency bins to follow the evolution, with providing a spectral energy distribution (SED) at each timestep. We adopt the standard 100 frequency bins ranging over 1 – 50,000 Å. Bolometric light curves are produced, integrating the SED at each time step. Light curves with any filter could be calculated by convolving the SED with the corresponding response function. In this paper, we present light curves in the  $g$ ,  $r$ , and  $i$

bands of SDSS,  $U$ ,  $B$ , and  $V$  bands of Johnson-Cousins system,  $UVW2$ ,  $UVM1$ ,  $UVW1$ ,  $U$ ,  $B$ , and  $V$  bands of Swift/UVOT and unfiltered observation of T. Noguchi<sup>15</sup>. While the ZTF  $gri$  filters are similar but not identical to the SDSS system (E. C. Bellm et al. 2018), given the small differences in the transmission curves, we adopt the SDSS filter functions in the comparison with ZTF photometry.

We obtain photospheric velocity ( $v_{\text{ph}}$ ) evolution for each light-curve model. The photosphere is defined as the location where the Rosseland mean optical depth becomes 2/3.

## 4. RESULTS

### 4.1. ECSN candidates

We explore ECSN candidates among the SN II sample with the light-curve diagnostic proposed by M. Sato et al. (2024), adopting the  $t_{\text{PT}}$ ,  $(g - r)_{t_{\text{PT}}/2}$ , and  $(B - V)_{t_{\text{PT}}/2}$  presented in Section 2.

Figure 2 shows the diagnostic of the SNe II with the color indices  $g - r$  and  $B - V$ . We identify ASASSN-14ha, SNe 2018zd, 2019amt, 2019lkx, 2019nzy, 2019pkh, 2021cwe, 2021hse, 2022mxv, and 2023axu as photometric ECSN candidates. For ASASSN-14ha and SN 2023axu,  $g - r$  satisfies Equation (1) whereas  $B - V$  does not satisfy Equation (2), but we retain them as we regard objects satisfying either color criterion as photometric candidates. Among the normal SNe II, we highlight three well-observed events (SNe 2005cs, 2013fs, and 2014cy) that span the plateau-luminosity range, as reference objects for comparison.

We next examine the spectra of the photometric ECSN candidates around  $t_{\text{PT}}/2$  to search for signatures of strong CSM interaction. Figure 3 shows optical spectra of SN 2018zd (J. Zhang et al. 2020) and ASASSN-14ha at epochs closest to  $t_{\text{PT}}/2$  (68.1 and 64.3 days, respectively), together with two representative spectra showing narrow lines: the flash spectrum of the Type-II SN 2013fs at  $\sim 0.8$  days since explosion (O. Yaron et al. 2017) and a spectrum of the Type-IIIn SN 2005ip at  $\sim 48$  days since discovery (M. Stritzinger et al. 2012). Since SN 2005ip likely exploded 8 – 10 days before discovery (N. Smith et al. 2009), the spectrum approximately corresponds to  $\sim 60$  days after explosion. These spectra were taken from WISeREP (O. Yaron & A. Gal-Yam 2012). For SN 2023axu, no spectra around  $t_{\text{PT}}/2$  are available in WISeREP, so we refer to M. Shrestha et al. (2024). ASASSN-14ha, SNe 2018zd, and

<sup>15</sup> For the observations by T. Noguchi, we adopt the quantum-efficiency curve of the MicroLine ML0261E.

**Table 1.** Parameter sets for the light-curve modeling of ECSN candidates (Step 1)

$M_{\text{env}}$	$X(\text{H})_{\text{env}}$	R	Mass cut	$E_{\text{exp}}$	$M(^{56}\text{Ni})$	$\dot{M}$	$r_{\text{CSM}}$	$v_0$	$v_{\infty}$	$\beta$
$[M_{\odot}]$		$[10^{13} \text{ cm}]$	$[M_{\odot}]$	$[10^{50} \text{ ergs}]$	$[M_{\odot}]$	$[M_{\odot} \text{ yr}^{-1}]$	$[\text{cm}]$	$[\text{km s}^{-1}]$	$[\text{km s}^{-1}]$	
2.0	0.7	6.5	1.366 – 1.370	0.2 – 14.2	0.002 – 0.003	$10^{-6} - 10^{-2}$	$10^{14} - 10^{16}$	1 – 5	10	1 – 5
3.0	0.2	7.0	1.364 – 1.370	0.2 – 13.3	0.002 – 0.003	$10^{-6} - 10^{-2}$	$10^{14} - 10^{16}$	1 – 5	10	1 – 5
3.0	0.5	7.0	1.364 – 1.370	0.2 – 13.9	0.002 – 0.003	$10^{-4} - 10^{-2}$	$10^{14} - 10^{16}$	1 – 5	10	1 – 5
3.0	0.7	7.1	1.364 – 1.373	0.1 – 13.2	0.002 – 0.003	$10^{-6} - 10^{-2}$	$10^{14} - 10^{16}$	1 – 5	10	1 – 5
4.7	0.5	7.3	1.363 – 1.370	0.2 – 13.7	0.002 – 0.003	$10^{-6} - 3 \times 10^{-2}$	$10^{14} - 10^{16}$	1 – 5	10	1 – 5
4.7	0.7	7.2	1.363 – 1.373	0.2 – 13.7	0.002 – 0.003	$10^{-6} - 3 \times 10^{-1}$	$10^{14} - 10^{16}$	1 – 5	10	1 – 5

NOTE—  $M_{\text{env}}$  and  $X(\text{H})_{\text{env}}$  are the envelope mass and hydrogen abundance of the progenitor,  $R$  is the progenitor radius,  $E_{\text{exp}}$  is the explosion energy,  $M(^{56}\text{Ni})$  is the ejected  $^{56}\text{Ni}$  mass,  $\dot{M}$  is the mass-loss rate,  $r_{\text{CSM}}$  is the CSM radius,  $v_0$  is the initial velocity of the wind,  $v_{\infty}$  is the terminal velocity of the wind, and  $\beta$  is the acceleration parameter of the wind. Step 1 explores 2080 models in total.

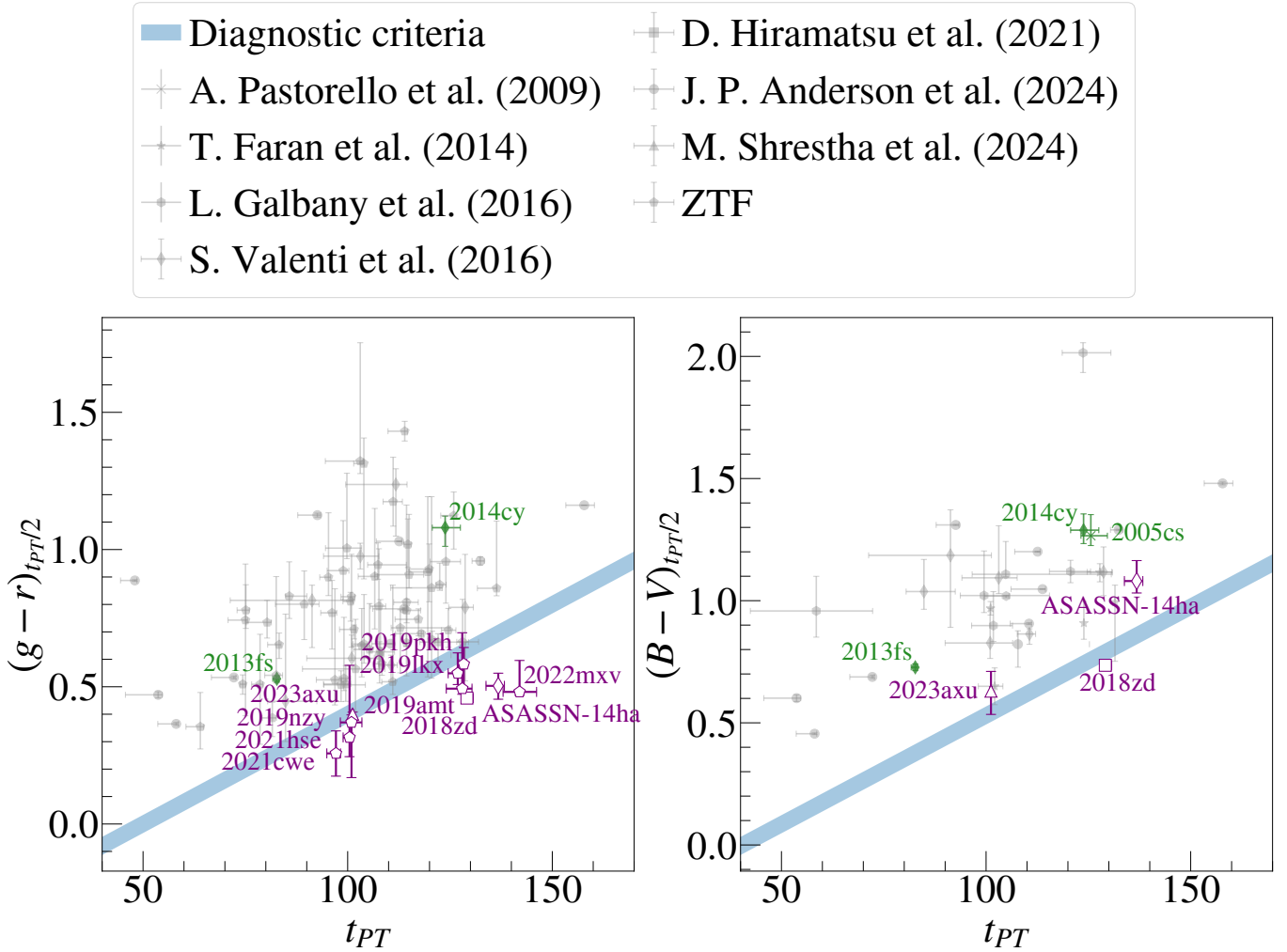


**Figure 2.** The diagnostic of the SNe II with the colors  $g-r$  and  $B-V$  in the left and right panels respectively. Purple points indicate the photometric ECSN candidates, i.e., objects bluer than the selection criteria in either  $g-r$  or  $B-V$  (M. Sato et al. 2024). Gray points indicate objects that are not bluer than the criteria in either color. The reference SNe are highlighted in green.

2023axu show no narrow lines around  $t_{PT}/2$ , indicating the absence of strong CSM interaction, and we designate them as the *gold candidates*. The remaining photometric ECSN candidates without spectra are treated as the *silver candidates*.

The estimated  $M(^{56}\text{Ni})$  for ASASSN-14ha, SNe 2018zd, and 2023axu in the literature are  $0.0014 \pm 0.0002$ ,  $0.0086 \pm 0.0005$ , and  $0.058 \pm 0.017 M_{\odot}$ , respectively (S. Valenti et al. 2016; D. Hiramatsu et al. 2021; M. Shrestha et al. 2024). Since no previous  $M(^{56}\text{Ni})$  estimates are available for the silver candidates, we estimate  $M(^{56}\text{Ni})$  from their tail  $g$  and  $r$  photometry (Section 2.2). We obtain  $M(^{56}\text{Ni}) = 0.2 \pm 0.02$ ,  $0.1 \pm 0.01$ ,  $0.09 \pm 0.003$ , and  $0.1 \pm 0.01 M_{\odot}$  for SNe 2019amt, 2019lkx, 2019pkh, and 2021cwe, with the uncertainties reflecting the photometric errors. For SNe 2019nzy, 2021hse, and 2022mxv, we instead derive upper limits,  $M(^{56}\text{Ni}) \lesssim 0.3$ ,  $0.2$ , and  $0.03 M_{\odot}$ , respectively as there is no epoch with detections in both  $g$  and  $r$  after  $t_{PT} + 15$  days.

## 4.2. Photometric properties

### 4.2.1. Gold candidates

Figure 4 shows the observed  $V$ -band absolute-magnitude light curves and  $B - V$  evolutions of the *gold candidates*, compared with those of the reference SNe, including Swift observations. For visual clarity, markers are plotted only for epochs separated by  $\geq 3$  days. The large errors of ASASSN-14ha are due to the distance uncertainty toward the host galaxy, with the distance modulus ranging from 29.53 (S. Valenti et al. 2016) to 30.86 (Ó. Rodríguez 2022).

While the plateau length of ASASSN-14ha is around 140 days, significantly longer than those of SNe 2005cs ( $\sim 100 - 130$  days), 2013fs ( $\sim 80 - 100$  days), and 2014cy ( $\sim 120$  days), those of SNe 2018zd and 2023axu are around 120 and 100 days, respectively, comparable to the reference SNe.

The plateau of ASASSN-14ha is faint,  $V \sim -15$  mag, slightly brighter than that of the low-luminosity SN 2005cs ( $V \sim -14.5$  mag) but still fainter than that of the normal SNe 2013fs ( $V \sim -17$  mag) and 2014cy ( $V \sim -15.5$  mag). The plateau brightness of SNe 2018zd and 2023axu is  $V \sim -16$  and  $-17$  mag, respectively, similar to that of the normal SNe 2013fs and 2014cy.

The tail of ASASSN-14ha is faint,  $V \sim -11$  mag around 150 days, brighter than that of SN 2005cs ( $V \sim -10$  mag around 150 days) but fainter than that of SNe 2013fs ( $V \sim -14.5$  mag around 100 days) and 2014cy ( $V \sim -12$  mag around 160 days). The tail of SN 2018zd ( $V \sim -11.5$  mag at  $\sim 180$  days) is sim-

ilar to that of SN 2014cy, while the tail of SN 2023axu ( $V \sim -15$  mag at  $\sim 100$  days) is comparable to that of SN 2013fs. The estimated  $M(^{56}\text{Ni})$  for the reference SNe 2005cs, 2013fs, and 2014cy are  $0.0021 \pm 0.0002$ ,  $0.0545 \pm 0.0003$ , and  $0.0037 \pm 0.0038 M_{\odot}$ , respectively. Together with the  $M(^{56}\text{Ni})$  estimates for ASASSN-14ha, SNe 2018zd, and 2023axu in Section 4.1, these estimates are broadly consistent with the  $V$ -band absolute magnitudes observed during the tails.

While ECSNe are theoretically predicted to produce a small amount of  $^{56}\text{Ni}$ ,  $0.002 - 0.004 M_{\odot}$  (F. S. Kitaura et al. 2006; H.-T. Janka et al. 2008; S. Wanajo et al. 2009), the tail-based  $M(^{56}\text{Ni})$  estimate for SN 2023axu is comparatively large. However, additional energy sources such as CSM interaction or pulsar spin-down can also power a luminous tail without necessarily affecting the plateau, as suggested for SN 1054 (T. J. Moriya et al. 2014; N. Tominaga et al. 2013). In such cases, the true  $M(^{56}\text{Ni})$  may be lower than that inferred under the assumption that the tail is powered solely by radioactive decay. We therefore do not rule out SN 2023axu from the candidates.

The  $B - V$  evolutions of the *gold candidates* are similar to those of the reference SNe before  $\sim 20$  days after explosion. During the plateau phase thereafter, the *gold candidates* are persistently bluer than SNe 2005cs and 2014cy on average. While the *gold candidates* show similar  $B - V$  evolutions to SN 2013fs, their plateau durations are longer than that of SN 2013fs, suggesting that both the color evolution and plateau length are important for distinguishing ECSN candidates from normal SNe II.

### 4.2.2. Silver candidates

Figures 5 and 6 show the observed  $r$ -band absolute-magnitude light curves of the *silver candidates*, compared with those of SNe 2013fs and 2014cy and the  $V$ -band light curve of SN 2005cs. For visual clarity, markers are plotted only for epochs separated by  $\geq 3$  days.

The plateau lengths of SNe 2019amt, 2019nzy, 2019pkh, 2021cwe and 2021hse are around 100 - 120 days, longer than SN 2013fs and consistent with SNe 2005cs and 2014cy. In contrast, the plateau lengths of SNe 2019lkx and 2022mxv are around 130 and 140 days, respectively, significantly longer than the reference SNe.

The plateaus of SNe 2019lkx, 2019nzy, 2021cwe, and 2021hse are of similar brightness ( $r \sim -17$  mag) to those of SN 2013fs and brighter than those of SNe 2005cs and 2014cy. Those of SNe 2019amt and 2022mxv are brighter ( $r \sim -17.5$  mag) than those of the reference SNe, suggesting that they belong to the brighter end

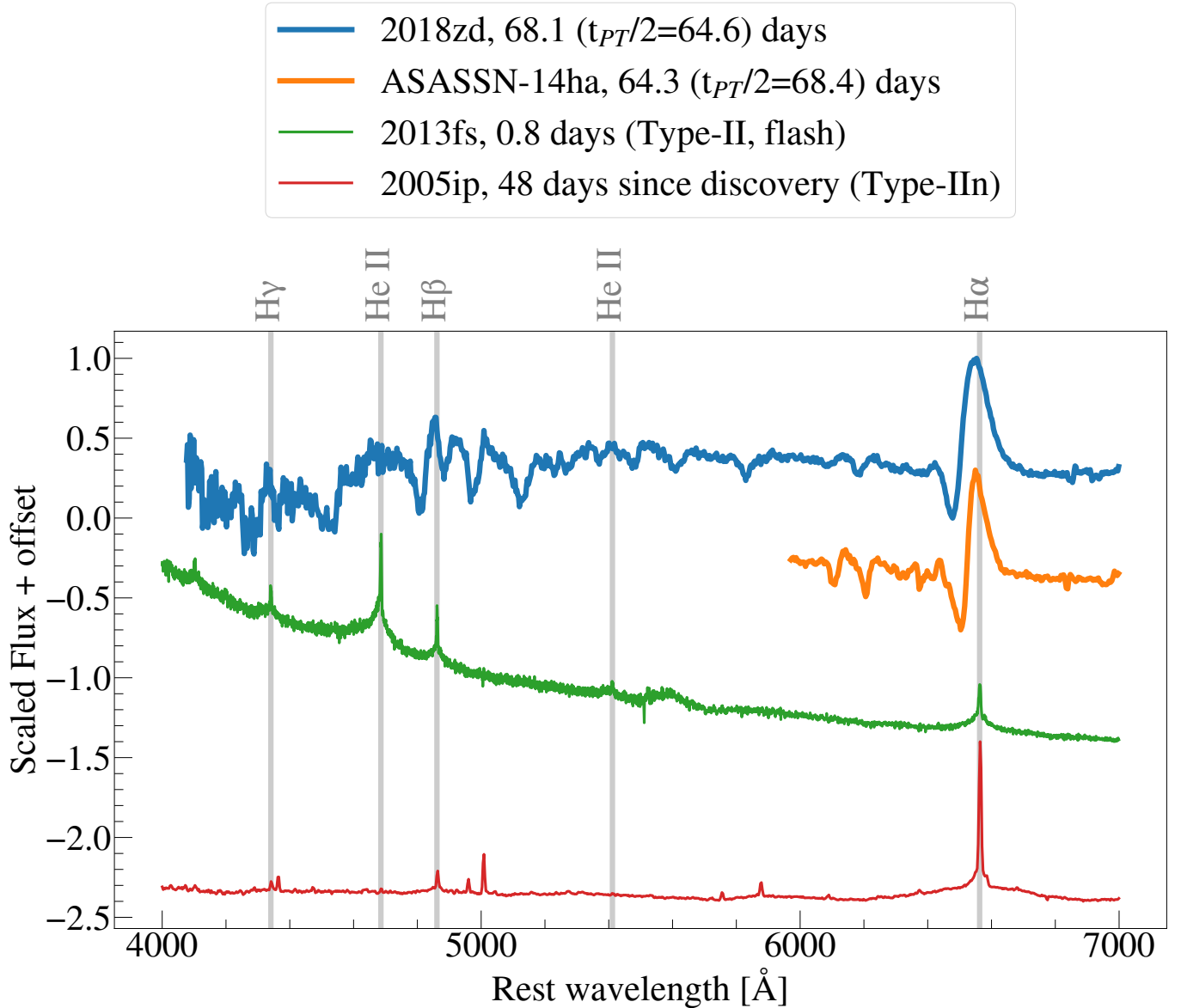


**Figure 3.** Spectra of SN 2018zd (thick blue line) and ASASSN-14ha (thick orange line) around  $t_{PT}/2$ . The flash spectrum of Type-II SN 2013fs (thin green line) and a spectrum of the Type-IIIn SN 2005ip (thin red line) are also shown as representatives of spectra with narrow lines due to CSM interaction. All spectra are obtained from WISeREP.

of the SN II population. The brightness evolution of SN 2019pkh in the plateau is somewhat peculiar, faint in the early phase ( $r \sim -15.5$  mag around 5 days) and gradually increasing toward the end of the plateau ( $r \sim -16.5$  mag around 110 days), possibly due to the increase of the photospheric radius, as seen in some low-luminosity SNe (G. Valerin et al. 2022).

The tails of SNe 2019amt, 2019lkx, 2019pkh, and 2021cwe are  $r \sim -16$  mag around 130 days, likely similar to SN 2013fs and brighter than SNe 2005cs and 2014cy, with SNe 2019pkh and 2021cwe showing bumpy evolution around 150 days, possibly due to interaction with a CSM of complex structure. The tail of SN 2019nzy is

$r \sim -17$  mag around 170 days, brighter than those of the reference SNe. The tail of SN 2022mxv is  $r \sim -13.5$  mag around 140 days, brighter than SNe 2005cs and 2014cy and fainter than SN 2013fs.

These bright tails of the *silver candidates* result in the  $M(^{56}\text{Ni})$  estimates similar to or higher than the  $M(^{56}\text{Ni})$  estimates for the reference SNe. The tail-based  $M(^{56}\text{Ni})$  estimates are also higher than the theoretical predictions (F. S. Kitaura et al. 2006; H.-T. Janka et al. 2008; S. Wanajo et al. 2009), possibly indicating that they are not ECSNe or that their tails are powered by additional sources, most plausibly CSM interaction and/or a central engine. Because spectra around  $t_{PT}/2$  are un-

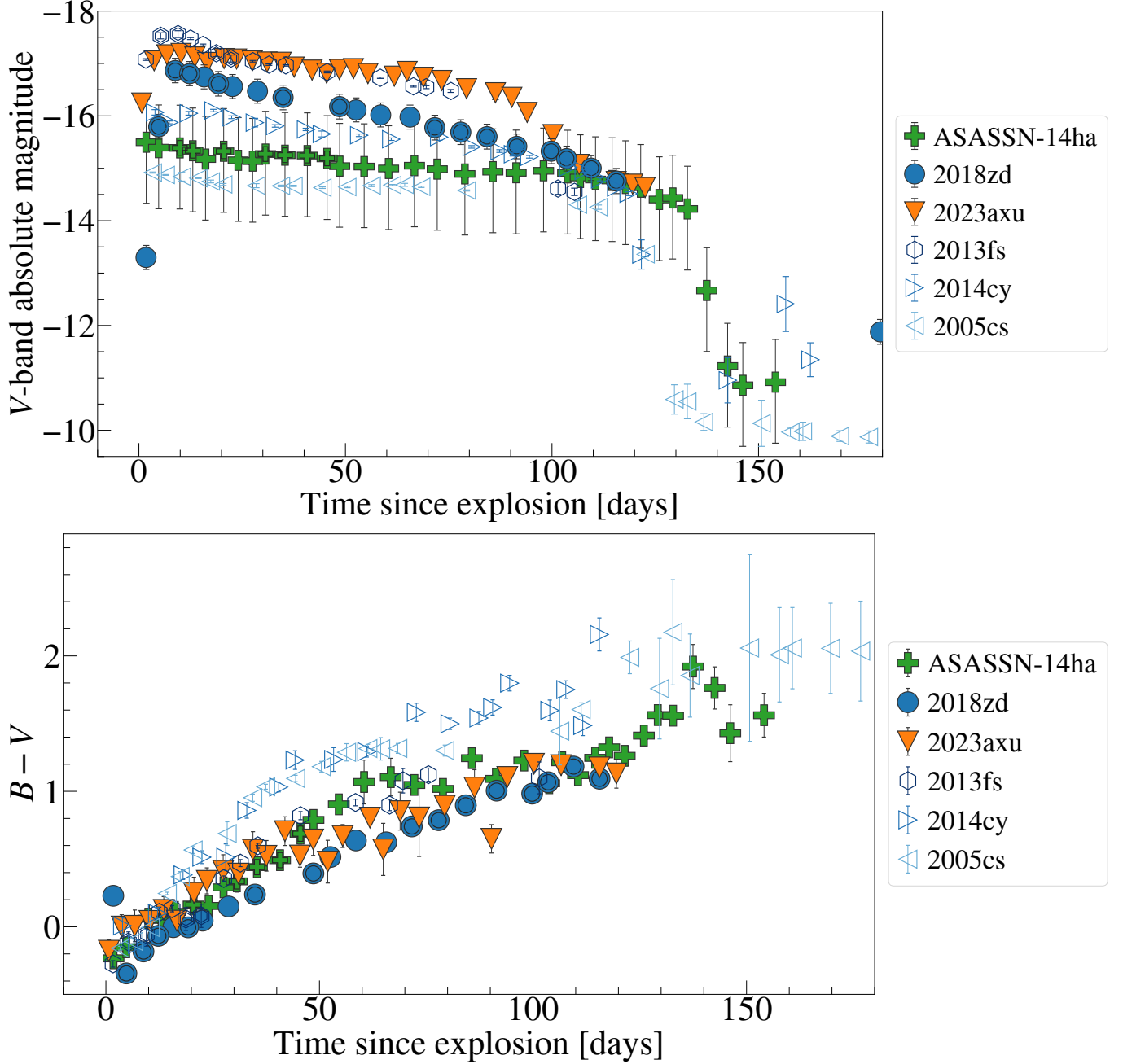


**Figure 4.** The observed  $V$ -band absolute-magnitude light curves (*top*) and  $B - V$  evolutions (*bottom*) of the *gold candidates*, ASASSN-14ha, SNe 2018zd, and 2023axu, together with the reference SNe 2005cs, 2013fs, and 2014cy. Ground-based observations are indicated by single marker edges, whereas Swift observations are indicated by double marker edges. Markers are shown only for epochs separated by  $\geq 3$  days to reduce crowding.

available for the *silver candidates*, we cannot distinguish these possibilities. Also, the tail brightness may be enhanced by a moderate CSM interaction that does not necessarily affect the plateau (T. J. Moriya et al. 2014). We therefore retain the *silver candidates* not as robust ECSN identifications, but as photometrically selected candidates that may include false positives, so as not to exclude potential ECSN candidates.

The  $g - r$  evolutions of the *silver candidates* during the plateau phase are, on average, bluer than that of SN 2014cy. Among them, SNe 2019amt and 2019pkh, show  $g - r$  evolutions comparable to SN 2013fs but with longer plateau durations. The remaining *silver candidates* are generally bluer than SN 2013fs.

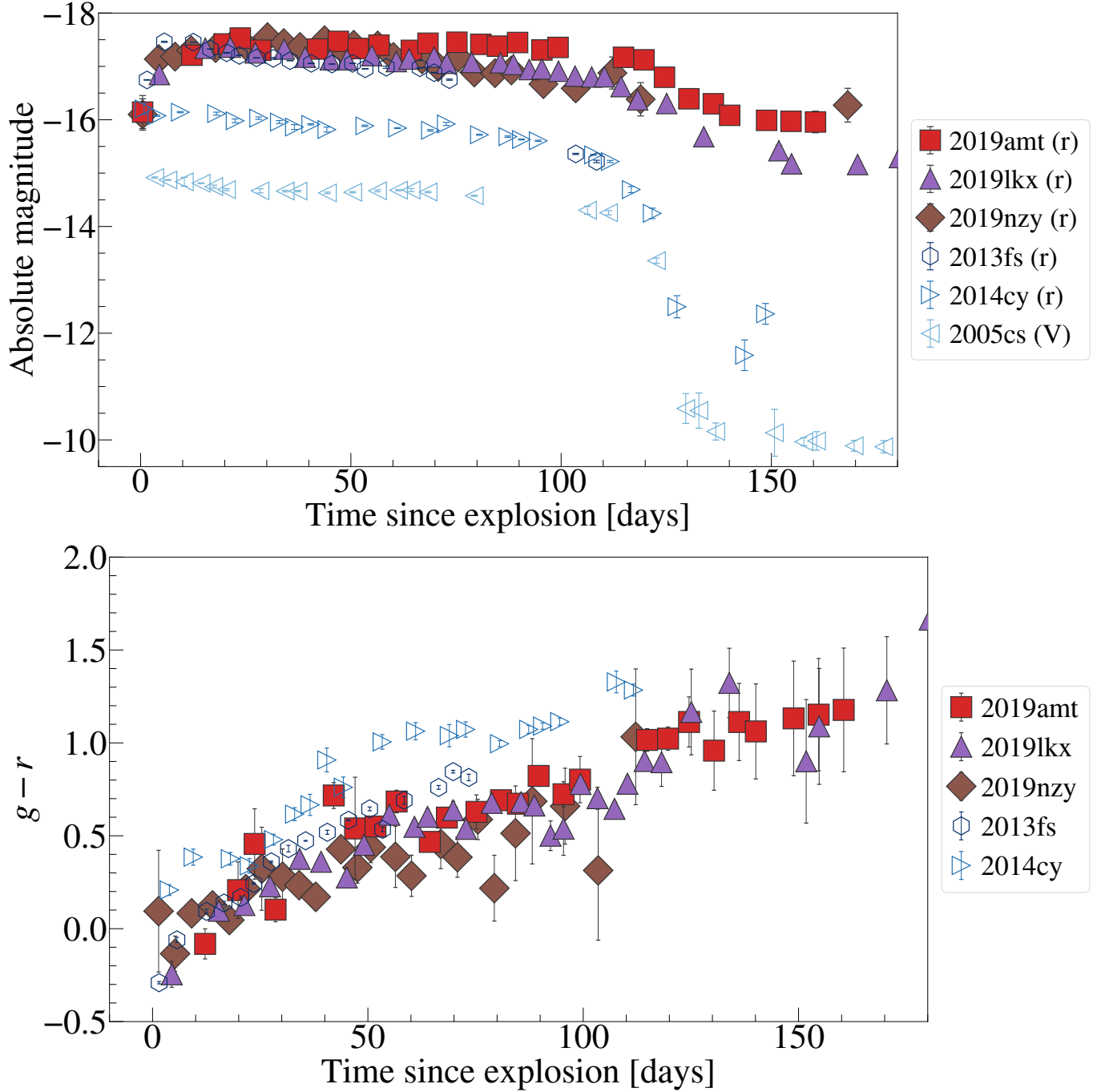


**Figure 5.** The observed  $r$ -band absolute-magnitude light curves (*top*) and  $g-r$  evolutions (*bottom*) of the *silver candidates*, SNe 2019amt, 2019lhx, and 2019nzy, together with those of the reference SNe 2013fs and 2014cy. For comparison, the observed  $V$ -band absolute magnitude light-curve of the reference SN 2005cs is also shown in the *top* panel. Markers are shown only for epochs separated by  $\geq 3$  days to reduce crowding.

#### 4.3. Comparison with Light-Curve Models

Figures 7 and 8 compare the best-fitting ECSN light-curve models and the observed light curves of the *gold* and *silver candidates*, respectively. Table 2 summarizes the explosion and progenitor properties inferred from the best-fitting models.

While the models show good agreement with the observations for the *gold candidates*, they are more (SN 2023axu) or less (ASASSN-14ha and SN 2018zd) luminous than the observations just after the peak. This may indicate the existence of more complicated CSM profiles (e.g., aspherical profile as indicated for

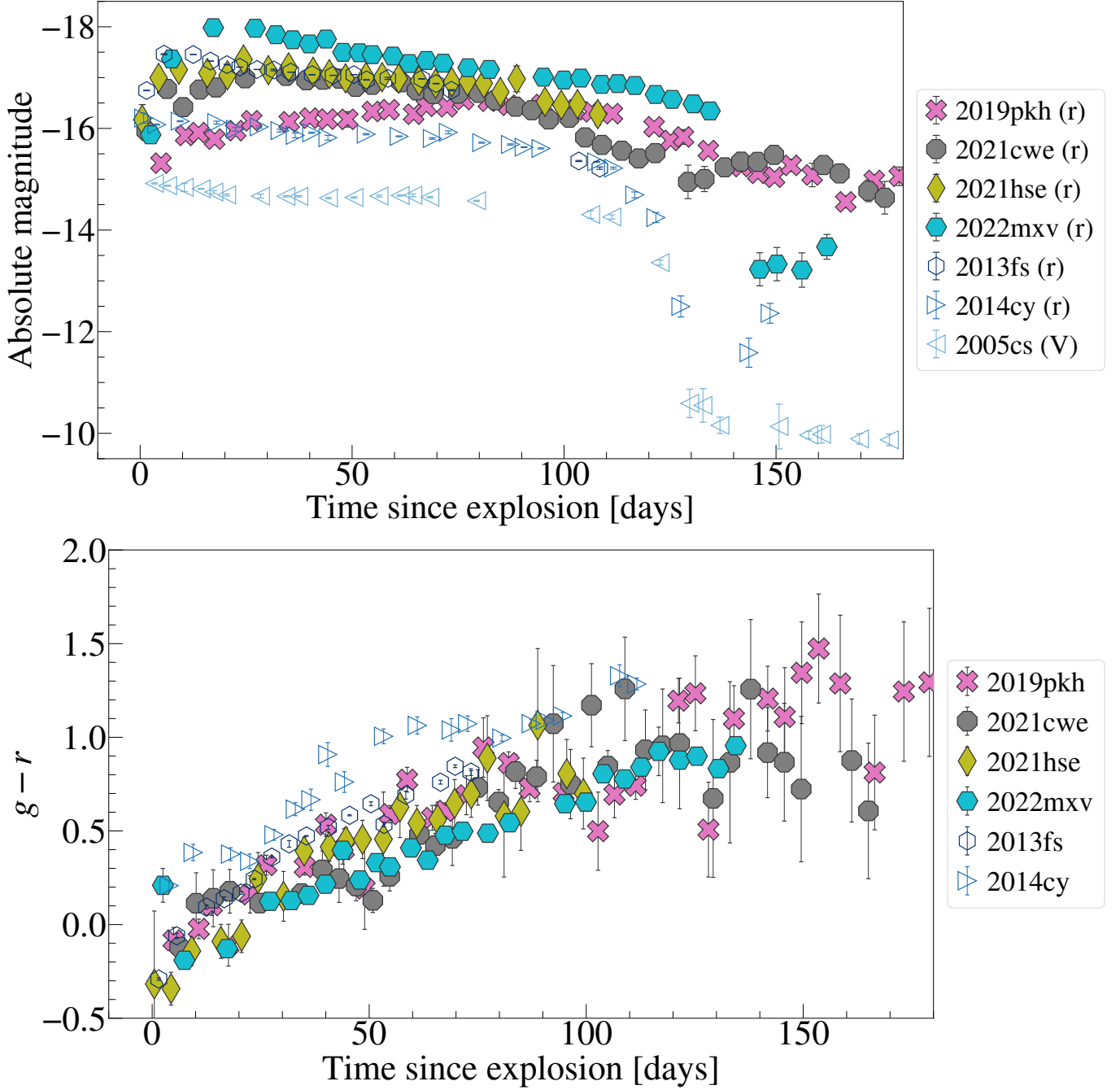


**Figure 6.** Same as figure 5, but for the *silver candidates*, SNe 2019pkh, 2021cwe, 2021hse, and 2022mxv.

SN 2023ixf; M. Shrestha et al. 2025; N. Smith et al. 2023; A. Singh et al. 2024) than considered here. On the other hand, since the peak luminosity reflects the overall density profile of the surrounding CSM, the agreement at the peak lends support to the inferred  $\dot{M}$  and  $v_0$  although they are degenerate. Also, since the duration and later-phase luminosity of plateaus reflect the properties of the H-rich envelopes of the progenitors and explosion energies (I. Y. Litvinova & D. K. Nadezhin 1985; D. V. Popov 1993; R. G. Eastman et al. 1994), the sim-

ilarities in the late plateaus lend support to the  $M_{\text{env}}$  and  $E_{\text{exp}}$  inferred here.

The observed  $v_{\text{H}\alpha}$  during the plateau phase of both ASASSN-14ha and SN 2018zd are around 2 – 3 times larger than the  $v_{\text{ph}}$  evolutions of the best-fitting model, while the detailed line formation cannot be directly derived from STELLA calculations. The relation between line velocities and  $v_{\text{ph}}$  has not been investigated for EC-SNe, whereas  $v_{\text{H}\alpha}/v_{\text{ph}} \sim 1 - 2$  is indicated for normal SNe II and SN 1987A due to the large H $\alpha$  optical depth

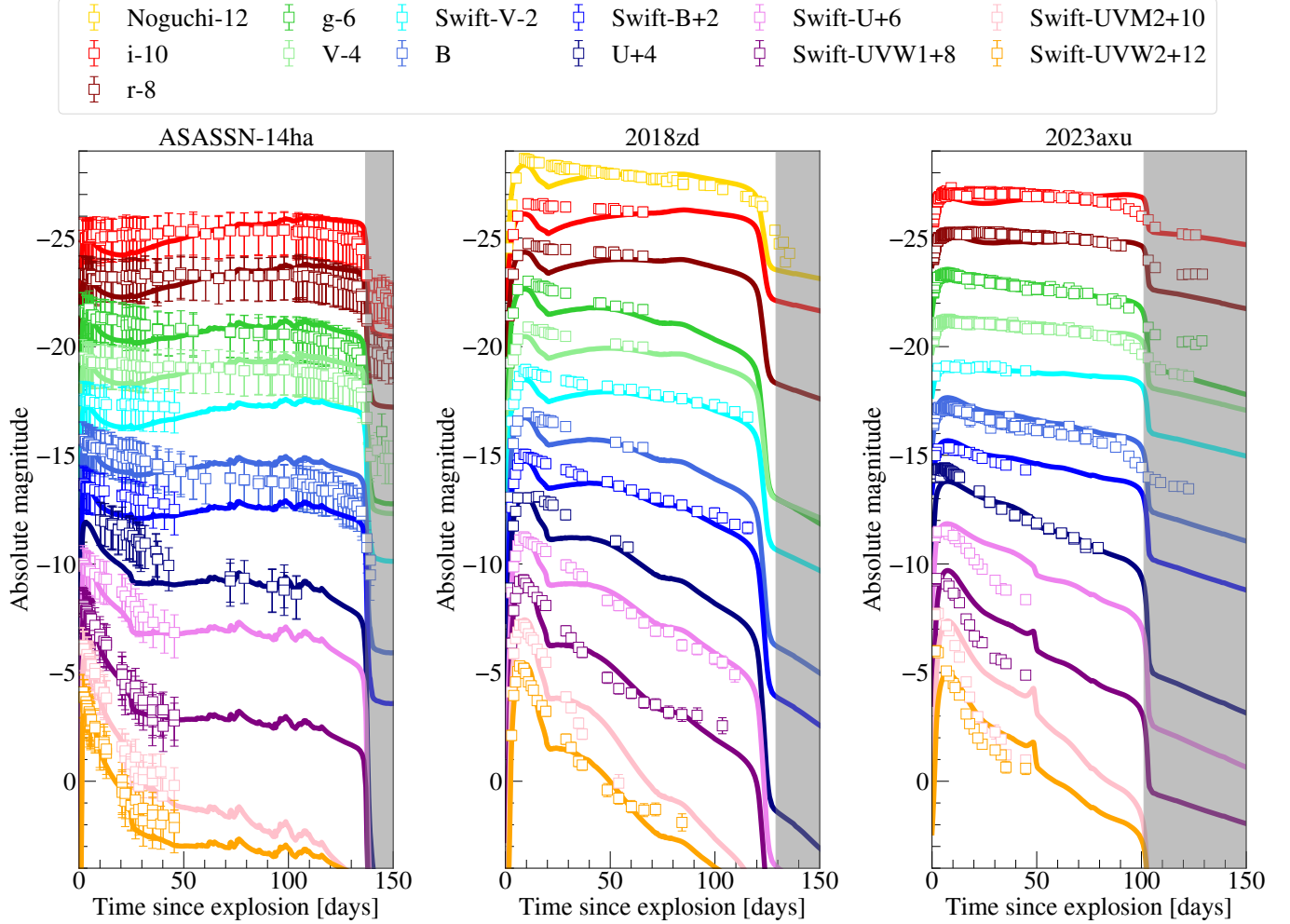


**Figure 7.** Comparison of the observed light curves (points) of the *gold candidates*, ASASSN-14ha (*left*), SNe 2018zd (*center*) and 2023axu (*right*) and the best-fitting ECSN multicolor light-curve models (lines). The gray-shaded region corresponds to epochs later than  $t_{PT}$  and is excluded from the  $\chi^2$  calculation.

above the electron-scattering photosphere (R. G. Eastman & R. P. Kirshner 1989; V. P. Utrobin & N. N. Chugai 2005; L. Dessart & D. J. Hillier 2005), which likely lies around the H recombination front. While  $v_{Fe\ II}/v_{ph} \sim 0.9 - 1.1$  is indicated for normal SNe II (L. Dessart & D. J. Hillier 2005), the observed  $v_{Fe\ II}$  for ASASSN-14ha and SN 2018zd are also significantly higher than the model  $v_{ph}$  ( $v_{Fe\ II}/v_{ph} \sim 2 - 3$  and  $\sim 1.5 - 2.5$ , respectively). In ECSNe, the photospheric radius may be smaller than the radius of the H recombination front due to the low ejecta density, while both radii tend to be closer in FeCCSNe (M. Sato et al. 2024). Therefore, if the line absorption in  $H\alpha$  and Fe II is dominated at and above the H recombination front, these velocity ratios may be higher in ECSNe than in normal SNe II. In particular for  $H\alpha$ , the optical depth may be suppressed in the highly ionized layers below the H recombination front, so that the absorption minimum can

be set at larger radii, as it traces the region where the line optical depth becomes significant (D. Kasen et al. 2001; L. Dessart & D. J. Hillier 2005).

For the *silver candidates*, the models are broadly consistent with the observations. For SNe 2019lhx and 2022mxv, although the models are fit only to the plateaus (from  $t_{exp}$  to  $t_{PT}$ ), they tend to favor extended CSM distributions ( $r_{CSM} = 3 \times 10^{15}$  cm) that would continue to affect the luminosity into the tails. This may indicate that the blue colors observed during the plateau are partly influenced by CSM interaction rather than being intrinsic to the SN ejecta. While we do not exclude them from the *silver candidates*, this possibility should be considered when interpreting their properties. By contrast, the other objects favor the models with less extended CSM ( $r_{CSM} \leq 10^{15}$  cm), for which the interaction ceases before the onset of the tail, and their late

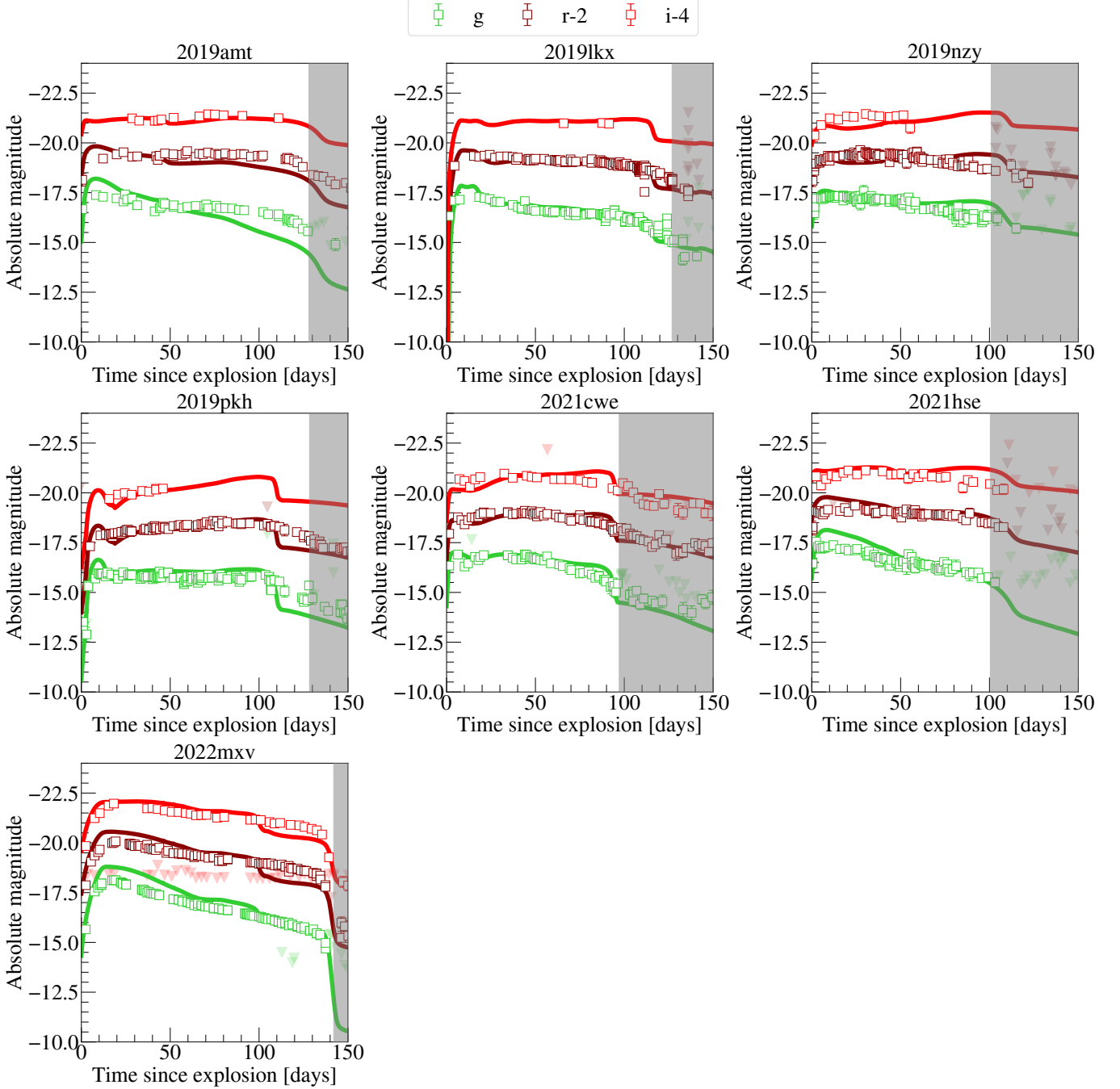


**Figure 8.** Comparison of the observed light curves (points) of the *silver candidates*, SNe 2019amt, 2019lkx, 2019nzy, 2019pkh, 2021cwe, 2021hse, and 2022mxv and the best-fitting ECSN multicolor light-curve models (lines). The gray-shaded region corresponds to epochs later than  $t_{PT}$  and is excluded from the  $\chi^2$  calculation.

plateaus show overall good agreements with the observations without invoking strong CSM effects.

## 5. DISCUSSION

### 5.1. Properties of the ECSN Candidates

The  $M_{env}$  inferred for the *gold candidates* are  $4.7 M_{\odot}$  (or  $3.0\text{--}4.7 M_{\odot}$  when the *silver candidates* are included; Table 2), indicating a lack of progenitors with either very

massive or very low-mass envelopes. Given the progenitor mass range of super-AGB stars ( $\sim 8\text{--}10 M_{\odot}$ ), this may suggest that their mass loss is extensive enough to strip a large fraction of the envelope, preventing the presence of progenitors with high envelope masses. Conversely, if the mass loss is strong enough to leave only a low-mass envelope, the progenitor is likely to be embedded in a dense and extended CSM, and the resulting

**Table 2.** Properties of the ECSN candidates, inferred from the multicolor light-curve modelings

SN Name	$M_{\text{env}}$	$X(\text{H})_{\text{env}}$	$E_{\text{exp}}$	$\dot{M}$	$r_{\text{CSM}}$	$v_0$	$v_\infty$	$\beta$	CSM mass
	$[M_\odot]$		$[10^{50} \text{ ergs}]$	$[M_\odot \text{ yr}^{-1}]$	$[10^{14} \text{ cm}]$	$[\text{km/s}]$	$[\text{km/s}]$		$[M_\odot]$
ASASSN-14ha	4.7	0.7	0.4	$3 \times 10^{-3}$	3	5	10	5	0.04
2018zd	4.7	0.7	0.8	$3 \times 10^{-2}$	3	5	10	5	0.40
2023axu	4.7	0.7	1.7	$10^{-2}$	10	5	10	2	0.37
2019amt	4.7	0.7	1.8	$10^{-2}$	10	5	10	1	0.34
2019lkx	4.7	0.7	1.7	$3 \times 10^{-3}$	30	5	10	1	0.30
2019nzy	3.0	0.7	1.4	$10^{-2}$	10	5	10	3	0.40
2019pkh	3.0	0.7	0.8	$3 \times 10^{-2}$	3	5	10	3	0.38
2021cwe	3.0	0.7	1.4	$3 \times 10^{-3}$	10	5	10	3	0.12
2021hse	3.0	0.7	1.3	$10^{-2}$	10	5	10	1	0.34
2022mxv	4.7	0.7	2.7	$10^{-2}$	30	5	10	3	1.07

explosion would more likely be classified as a Type IIn SN, as discussed in the context of the faint-fast subclass by D. Hiramatsu et al. (2024), rather than an ordinary SN II, which may explain the apparent absence of progenitors with low envelope masses in our sample.

Figure 9 shows the distribution of the  $E_{\text{exp}}$  inferred for the ECSN candidates, together with the median values inferred for normal SNe II in L. Martínez et al. (2022); B. M. Subrayan et al. (2023); K. K. Das et al. (2025b) and the canonical ECSN explosion energy of  $10^{50}$  erg (F. S. Kitaura et al. 2006; H.-T. Janka et al. 2008). The  $E_{\text{exp}}$  inferred for the ECSN candidates are  $(0.4 - 1.7) \times 10^{50}$  erg for the *gold candidates* and  $(0.4 - 2.7) \times 10^{50}$  erg including the *silver candidates*, less energetic than the median values inferred for normal SNe II. This is broadly consistent with first-principles simulations, which find that ECSNe can achieve shock revival with less neutrino heating than FeCCSNe owing to the steep density gradient at the super-AGB core surface, leading to low explosion energies ( $\sim 10^{50}$  erg; F. S. Kitaura et al. 2006; H.-T. Janka et al. 2008).

The inferred  $r_{\text{CSM}}$  and  $\dot{M}$  ranges are  $(3-10) \times 10^{14}$  cm and  $3 \times 10^{-3} - 3 \times 10^{-2} M_\odot \text{ yr}^{-1}$ , respectively, for the *gold candidates*, assuming  $v_\infty = 10 \text{ km s}^{-1}$ . The  $\dot{M}$  is much greater than that at the beginning of the thermal pulse phase,  $\sim (2-3) \times 10^{-5} M_\odot \text{ yr}^{-1}$ , predicted by stellar evolution calculations (M. Limongi et al. 2024). The compact  $r_{\text{CSM}}$  indicates that such strong mass loss lasts  $\sim 10 - 20$  years before the explosions and thus occurred during the very final stage in the super-AGB phase, lasting typically  $\sim 10^4 - 10^5$  years (C. L. Doherty et al. 2017). This enhancement of  $\dot{M}$  is possibly related to the decreasing interpulse period as the core approaches the Chandrasekhar mass (A. J. T. Poelarends et al. 2008).

Given that the tail-based  $M(^{56}\text{Ni})$  may be overestimated, we test the sensitivity of our results by using the models in Step 1, which adopt a theoretically expected  $M(^{56}\text{Ni})$  (S. Wanajo et al. 2009). The inferred properties are listed in Table 4 in Appendix B. The  $M_{\text{env}}$  are unchanged or increased from 3.0 to 4.7  $M_\odot$  and the  $E_{\text{exp}}$  are unchanged or decreased by up to factor of two. These  $M_{\text{env}}$  and  $E_{\text{exp}}$  changes are required to maintain plateau length and brightness with less  $^{56}\text{Ni}$  heating. The  $\dot{M}$  and  $r_{\text{CSM}}$  are unchanged or changed by factors of three. These unchanged or modestly changed properties indicate that our discussion based on the inferred  $M_{\text{env}}$ ,  $E_{\text{exp}}$ ,  $\dot{M}$ , and  $r_{\text{CSM}}$  is essentially unchanged within plausible uncertainties in  $M(^{56}\text{Ni})$ .

## 5.2. Occurrence Rate

With the use of the obtained ECSN candidates, we estimate a volumetric rate for ECSNe. In this work, the *silver candidates* are drawn exclusively from the ZTF survey sample, whereas the *gold candidates* are drawn exclusively from the literature sample. While the ZTF survey sample provides a systematic data set, strong CSM interaction cannot be excluded for the *silver candidates*, and they may include false positives. We therefore use the *silver candidates* to derive an upper limit on the ECSN occurrence ratio among SNe II. In contrast, while the literature sample is heterogeneous, it contains more robust *gold candidates*. Thus, we use the *gold candidates* to derive a lower limit on the ECSN occurrence ratio among SNe II.

We exclude SNe 2005cs, 2018zd, and 2023axu from the literature sample in the rate discussion to obtain a more uniform sample, since they were selected based on prior interest. After this exclusion, the literature sample contains 33 SNe II, among which we identify one *gold*

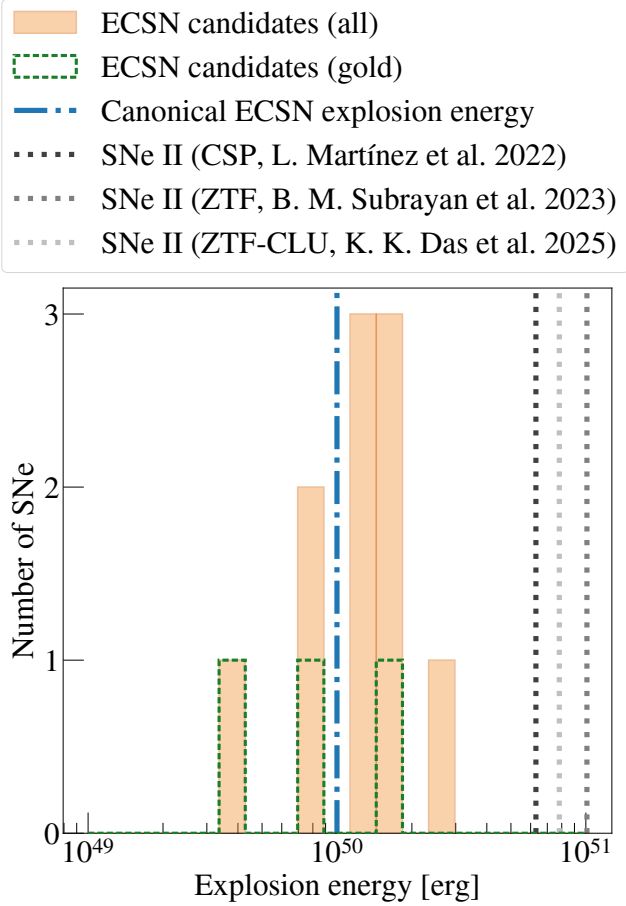


**Figure 9.** The distribution of the  $E_{\text{exp}}$  inferred for the ECSN candidates (the *gold candidates* in green dotted line and the *silver candidates* in orange), together with the median values of the  $E_{\text{exp}}$  of normal SNe II (gray dotted lines) from literature (L. Martínez et al. 2022; B. M. Subrayan et al. 2023; K. K. Das et al. 2025b) and the canonical ECSN explosion energy of  $10^{50}$  erg (blue dash-dotted line; F. S. Kitaura et al. 2006; H.-T. Janka et al. 2008).

*candidate*, ASASSN-14ha. This gives an ECSN occurrence ratio among SNe II,  $r(\frac{\text{ECSN}}{\text{SN II}})$ , of  $3.0^{+10.6}_{-2.9}$  % with the uncertainties corresponding to the central 90% confidence interval for a binomial proportion. We interpret this as a lower-limit constraint.

For the ZTF survey sample, we use the  $r$ -band photometry and apply a volume correction using the  $1/V_{\text{max}}$  method (M. Schmidt 1968) as done by K. K. Das et al. (2025a); M. Tanaka et al. (2016); N. Tominaga et al. (2019); S. Toshikage et al. (2024). Each object is weighted by  $1/V_{\text{max}} = 1/D_{\text{max}}^3$ , where  $D_{\text{max}}$  is the furthest distance at which the transient can be detected given the limiting magnitude, which is  $r = 20.6$  mag for ZTF (F. J. Masci et al. 2019). Since our sample is required to be detected around  $t_{\text{PT}}$ , we adopt  $1/V_{\text{max}}$  method using the brightness at  $t_{\text{PT}}$  estimated from the

linear interpolation or extrapolation of the observed photometry. While K. K. Das et al. (2025a) correct for the spectroscopic completeness and the ZTF pipeline recovery efficiency factor as well, we do not as it is difficult to evaluate them for our complicated selection criteria. After the volume correction,  $r(\frac{\text{ECSN}}{\text{SN II}})$  is estimated as  $15.7^{+17.3}_{-12.7}$  % from the *silver candidates*, where the uncertainties correspond to the central 90% confidence interval from bootstrap resampling of the  $1/V_{\text{max}}$ -weighted sample. We interpret this as an upper-limit constraint.

With the representative  $r(\frac{\text{ECSN}}{\text{SN II}})$  range, 3.0 – 15.7 % from the *gold* and *silver candidates*, we next discuss the ECSN ratio among CCSNe,  $r(\frac{\text{ECSN}}{\text{CCSN}})$ , the occurrence rate of ECSNe,  $R_{\text{ECSN}}$ , and the initial-mass window for stars that explode as ECSNe,  $\Delta M_{\text{ECSN}}$ . Adopting the fraction of SNe II among CCSNe from the LOSS survey ( $\sim 58.3$  %, W. Li et al. 2011b), this corresponds to  $r(\frac{\text{ECSN}}{\text{CCSN}}) = 1.8 - 9.2$  %. This is broadly consistent with the estimate from a comparison of  $^{86}\text{Kr}$  abundance between the ECSN nucleosynthetic calculation and solar abundance ( $\leq 8.5$  %, S. Wanajo et al. 2018).

Combined with the volumetric rate of SNe II from the ZTF-CLU survey ( $3.9 \times 10^4 \text{ Gpc}^{-3} \text{ yr}^{-1}$ , K. K. Das et al. 2025a), the  $r(\frac{\text{ECSN}}{\text{SN II}})$  range gives a  $R_{\text{ECSN}}$  range of  $(1.2 - 6.1) \times 10^3 \text{ Gpc}^{-3} \text{ yr}^{-1}$ .

With the estimated  $r(\frac{\text{ECSN}}{\text{CCSN}})$ , we discuss the initial-mass window for stars that explode as ECSNe,  $\Delta M_{\text{ECSN}}$ . Assuming the Salpeter initial-mass function (IMF; E. E. Salpeter 1955), the  $r(\frac{\text{ECSN}}{\text{CCSN}})$  range corresponds to a progenitor mass window of  $0.1 \lesssim \Delta M_{\text{ECSN}} \lesssim 0.7 M_{\odot}$ , for an ECSN/FeCCSN boundary mass of  $8 - 10 M_{\odot}$ . The derived mass window is broadly consistent with the estimate by D. Hiramatsu et al. (2021),  $0.06 - 0.69 M_{\odot}$ .

We next discuss the effect of host-galaxy extinction. In this work, the literature sample from J. P. Anderson et al. (2014); L. Galbany et al. (2016) and the ZTF survey sample are not corrected for host-galaxy extinction. If a uniform host-galaxy extinction of  $E(B - V) = 0.1$  mag is assumed for these samples, the number of *silver candidates* increases to 14, whereas the number of *gold candidates* does not change. This difference between the *silver* and *gold candidates* is possibly due to the fact that nearby, spectroscopically well-observed objects that appear blue due to strong CSM interaction may be classified as SNe IIn, and are therefore less likely to remain in the literature SN II sample, whereas similar blue objects may remain near the selection criterion in the ZTF survey sample, where spectroscopic observations are typically less frequent and of lower resolution. The corresponding upper-side estimates are  $\sim 25.6$  % for  $r(\frac{\text{ECSN}}{\text{SN II}})$ ,  $\sim 14.9$  % for  $r(\frac{\text{ECSN}}{\text{CCSN}})$ ,

$\sim 1.0 \times 10^4 \text{ Gpc}^{-3} \text{ yr}^{-1}$  for  $R_{\text{ECSN}}$ , and  $\sim 1.1 M_{\odot}$  for  $\Delta M_{\text{ECSN}}$ , while the lower-side estimates remain unchanged. If  $\sim 10 - 20 \%$  of SNe II have host-galaxy extinction of  $E(B - V) \geq 0.1 \text{ mag}$  (e.g., K. K. Das et al. 2025a), this corresponds to  $\sim 6 - 12$  of 62 SNe II in the ZTF survey sample. This is comparable to the increase of the 7 *silver candidates* under the uniform  $E(B - V) = 0.1 \text{ mag}$  assumption, suggesting that the increase may not be much larger even if SNe II close to the ECSN selection criterion preferentially had such non-negligible extinction. Also, the increase of the 7 *silver candidates* under this assumption suggests that correction of host-galaxy extinction, e.g., with sufficiently high-resolution spectra or well-sampled multi-band photometry, is important for completely identifying possible ECSN candidates.

On the other hand, the upper-limit estimate can also be biased high by possible contamination from SNe II with blue colors caused by strong CSM interaction among the *silver candidates*. If SNe 2019amt, 2019lkx, 2019pkh, and 2021cwe are excluded, for which the bright tails may suggest high  $M(^{56}\text{Ni})$  or long-lasting CSM interaction, the  $r(\frac{\text{ECSN}}{\text{SN II}})$  from the *silver candidates* is  $11.6^{+16.9}_{-11.6} \%$ . This gives a  $r(\frac{\text{ECSN}}{\text{CCSN}})$  range of  $\sim 1.8 - 6.8 \%$ , a  $R_{\text{ECSN}}$  range of  $\sim (1.2 - 4.5) \times 10^3 \text{ Gpc}^{-3} \text{ yr}^{-1}$ , and a  $\Delta M_{\text{ECSN}}$  range of  $\sim 0.1 - 0.5 M_{\odot}$ . Also, if SNe 2019lkx and 2022mxv are excluded, for which the light-curve models infer the existence of extended CSM, the  $r(\frac{\text{ECSN}}{\text{SN II}})$  from the *silver candidates* is  $4.2^{+5.0}_{-3.0} \%$ . This gives a  $r(\frac{\text{ECSN}}{\text{CCSN}})$  range of  $\sim 1.8 - 2.5 \%$ , a  $R_{\text{ECSN}}$  range of  $\sim (1.2 - 1.7) \times 10^3 \text{ Gpc}^{-3} \text{ yr}^{-1}$ , and a  $\Delta M_{\text{ECSN}}$  range of  $\sim 0.1 - 0.2 M_{\odot}$ .

## 6. CONCLUSION

In this study, we have searched for ECSN candidates among previously reported SNe II in the literature and within the ZTF public results, using the color-based diagnostic proposed by M. Sato et al. (2024). We selected ten candidates and investigated their photometric properties in detail. By comparing the multicolor light curves with radiation-hydrodynamical models, we inferred physical properties for the candidates, with particularly reliable estimates for the *gold candidates*. The inferred explosion energies are  $(0.4 - 1.7) \times 10^{50} \text{ erg}$  for the *gold candidates* and  $(0.4 - 2.7) \times 10^{50} \text{ erg}$  including the *silver candidates*, consistent with first-principles predictions (F. S. Kitaura et al. 2006; H.-T. Janka et al. 2008). The inferred mass-loss rates are  $3 \times 10^{-3} - 3 \times 10^{-2} M_{\odot} \text{ yr}^{-1}$  for the *gold candidates* and remain the same if the *silver candidates* are included, higher than those predicted for the early super-AGB

phase (M. Limongi et al. 2024). We derived the observational implication for the ECSN occurrence ratio among SNe II,  $r(\frac{\text{ECSN}}{\text{SN II}})$ , of  $3.0^{+10.6}_{-2.9}$  and  $15.7^{+17.3}_{-12.7} \%$  from *gold* and *silver candidates*, respectively, which we interpret as the lower and upper limits, respectively. The estimate from the *silver candidates* may be affected by possible host-galaxy extinction and contamination by SNe II showing blue color due to a strong CSM interaction. The representative  $r(\frac{\text{ECSN}}{\text{SN II}})$  range,  $3.0 - 15.7 \%$ , corresponds to a range of ECSN occurrence ratio among CCSNe,  $r(\frac{\text{ECSN}}{\text{CCSN}}) = 1.8 - 9.2 \%$ , and a range of volumetric rate of ECSNe,  $R_{\text{ECSN}} = (1.2 - 6.1) \times 10^3 \text{ Gpc}^{-3} \text{ yr}^{-1}$ , which implies an initial mass window of  $0.1 \lesssim \Delta M_{\text{ECSN}} \lesssim 0.7 M_{\odot}$  for their progenitors, assuming the standard IMF (E. E. Salpeter 1955) and an ECSN/FeCCSN boundary mass of  $8 - 10 M_{\odot}$ .

We finally note an outlook. For the *silver candidates*, we cannot rule out contamination of SNe that appear blue due to strong CSM interaction, as spectra around  $t_{\text{PT}}/2$  are not available for these objects. Consequently, the allowed ranges of the ECSN occurrence rate and progenitor mass window remain relatively broad. This highlights the need for spectroscopic follow-up of future ECSN candidates, particularly around the middle of the plateau, to enable a more robust identification of EC-SNe.

## ACKNOWLEDGEMENTS

We thank the anonymous referee for helpful comments that improved the manuscript. We thank Yudai Suwa, Kazumi Kashiyama, Keiichi Maeda, Ken'ichi Nomoto, Marco Limongi, Masaomi Tanaka, José Prieto, Régis Cartier, and Jared Goldberg for helpful discussions and input. This work is supported by the Japan Society for the Promotion of Science Open Partnership Bilateral Joint Research Project between Japan and Chile (JPJSBP120239901, 120259901). MP is supported by the RSF grant 24-12-00141 for spectral analysis. Numerical computations were in part carried out on the general-purpose PC cluster at the Center for Computational Astrophysics, National Astronomical Observatory of Japan. This research has made use of the NASA/IPAC Infrared Science Archive, which is funded by the National Aeronautics and Space Administration and operated by the California Institute of Technology. The relevant IPAC/IRSA service DOI is 10.26131/IRSA539.

## APPENDIX

## A. THE OBSERVATIONAL PROPERTIES OF THE SNE II

The observational properties of the SNe II are summarized in Table 3.

**Table 3.** The Observational Properties of the SNe II

SN Name	$t_{\text{exp}}$ [MJD]	$t_{\text{PT}}$ [days]	$(g-r)_{t_{\text{PT}/2}}$ [mag]	$(B-V)_{t_{\text{PT}/2}}$ [mag]	Reference of photometry data
2005cs	$53548.50 \pm 0.25$	$125.6^{+1.9}_{-4.0}$ <i>a</i>	–	$1.27^{+0.09}_{-0.04}$	A. Pastorello et al. (2004)
1999gi	$51518.00 \pm 2.00$	$127.8^{+3.1}_{-3.1}$ <i>a</i>	–	$1.12^{+0.04}_{-0.04}$	T. Faran et al. (2014)
2000dj	$51788.00 \pm 3.50$	$123.9^d$	–	$0.91^{+0.09}_{-0.07}$	T. Faran et al. (2014)
2002gd	$52552.00$	$101.1^d$	–	$0.97^{+0.03}_{-0.03}$	T. Faran et al. (2014)
2003hl	$52867.00 \pm 2.50$	$131.5^d$	–	$0.99^{+0.07}_{-0.24}$	T. Faran et al. (2014)
2003iq	$52920.00 \pm 1.00$	$102.1^{+2.0}_{-2.0}$ <i>a</i>	–	$0.65^{+0.08}_{-0.08}$	T. Faran et al. (2014)
1986l	$46708.00 \pm 1.50$ <i>b</i>	$104.9^{+2.3}_{-0.7}$ <i>d</i>	–	$1.02^{+0.00}_{-0.01}$	L. Galbany et al. (2016)
1992af	$48798.80 \pm 4.00$ <i>b</i>	$58.5^{+8.1}_{-13.8}$ <i>d</i>	–	$0.96^{+0.14}_{-0.11}$	L. Galbany et al. (2016)
1999cr	$51246.50 \pm 2.00$ <i>b</i>	$101.8^{+1.3}_{-4.7}$ <i>d</i>	–	$0.90^{+0.14}_{-0.06}$	L. Galbany et al. (2016)
1999em	$51476.50 \pm 2.50$ <i>b</i>	$104.8^{+3.2}_{-25.8}$ <i>d</i>	–	$1.11^{+0.13}_{-0.01}$	L. Galbany et al. (2016)
2003bn	$52694.50 \pm 1.50$ <i>b</i>	$120.6^{+2.1}_{-4.9}$ <i>d</i>	–	$1.12^{+0.05}_{-0.05}$	L. Galbany et al. (2016)
2003bl	$52696.50 \pm 2.00$ <i>b</i>	$99.5^{+1.8}_{-16.0}$ <i>d</i>	–	$1.02^{+0.18}_{-0.07}$	L. Galbany et al. (2016)
2003hg	$52865.50 \pm 2.50$ <i>b</i>	$123.7^{+0.1}_{-6.8}$ <i>d</i>	–	$2.01^{+0.04}_{-0.08}$	L. Galbany et al. (2016)
2013bu	$56399.30 \pm 2.25$	$103.1^{+4.5}_{-4.5}$	$0.98^{+0.05}_{-0.05}$	$1.09^{+0.21}_{-0.06}$	S. Valenti et al. (2016)
2013fs	$56570.62 \pm 0.25$	$82.7^{+0.5}_{-0.5}$	$0.53^{+0.01}_{-0.01}$	$0.73^{+0.01}_{-0.01}$	S. Valenti et al. (2016)
lsq13dpa	$56642.20 \pm 1.00$	$128.7^{+2.0}_{-2.0}$	$0.79^{+0.19}_{-0.27}$	$1.12^{+0.10}_{-0.10}$	S. Valenti et al. (2016)
lsq14gv	$56674.30 \pm 1.00$	$84.8^{+2.4}_{-7.7}$	$0.45^{+0.32}_{-0.15}$	$1.04^{+0.13}_{-0.07}$	S. Valenti et al. (2016)
ASASSN-14dq	$56841.00 \pm 2.75$	$101.0^{+5.5}_{-5.5}$	$0.60^{+0.08}_{-0.01}$	$0.83^{+0.14}_{-0.06}$	S. Valenti et al. (2016)
2014cy	$56899.50 \pm 0.50$	$123.8^{+2.2}_{-3.7}$	$1.08^{+0.04}_{-0.07}$	$1.29^{+0.07}_{-0.05}$	S. Valenti et al. (2016)
ASASSN-14gm	$56900.50 \pm 0.75$	$110.6^{+1.5}_{-1.5}$	$0.58^{+0.04}_{-0.06}$	$0.86^{+0.02}_{-0.04}$	S. Valenti et al. (2016)
ASASSN-14ha	$56910.00 \pm 0.75$	$136.8^{+1.5}_{-1.5}$	$0.50^{+0.05}_{-0.05}$	$1.08^{+0.08}_{-0.05}$	S. Valenti et al. (2016)
2014dw	$56957.50 \pm 5.00$	$91.3^{+10.0}_{-10.0}$	$0.81^{+0.06}_{-0.17}$	$1.19^{+0.19}_{-0.29}$	S. Valenti et al. (2016)
2015W	$57024.50 \pm 5.00$	$111.8^{+2.3}_{-2.7}$	$1.24^{+0.06}_{-0.19}$	–	S. Valenti et al. (2016)
2018zd	$58178.41 \pm 0.05$	$129.1^{+0.5}_{-1.5}$ <i>d</i>	$0.46^{+0.00}_{-0.00}$	$0.74^{+0.00}_{-0.00}$	D. Hiramatsu et al. (2021)
2004dy	$53241.00 \pm 1.50$	$48.0^{+0.5}_{-0.5}$ <i>c</i>	$0.89^{+0.00}_{-0.00}$	–	J. P. Anderson et al. (2024)
2004er	$53271.80 \pm 1.00$	$157.8^{+2.5}_{-2.5}$ <i>c</i>	$1.16^{+0.00}_{-0.00}$	$1.48^{+0.01}_{-0.01}$	J. P. Anderson et al. (2024)
2004fc	$53293.50 \pm 0.50$	$132.4^{+1.0}_{-1.0}$ <i>c</i>	$0.96^{+0.01}_{-0.01}$	$1.29^{+0.00}_{-0.00}$	J. P. Anderson et al. (2024)
2005J	$53382.80 \pm 3.50$	$113.8^{+0.7}_{-0.7}$ <i>c</i>	$0.78^{+0.00}_{-0.00}$	$1.05^{+0.00}_{-0.00}$	J. P. Anderson et al. (2024)
2005dz	$53619.50 \pm 2.00$	$110.5^{+0.6}_{-0.6}$ <i>c</i>	$0.66^{+0.00}_{-0.00}$	$0.91^{+0.00}_{-0.00}$	J. P. Anderson et al. (2024)
2006Y	$53766.50 \pm 2.00$	$58.1^{+0.5}_{-0.5}$ <i>c</i>	$0.36^{+0.01}_{-0.01}$	$0.46^{+0.00}_{-0.00}$	J. P. Anderson et al. (2024)
2006ai	$53781.80 \pm 2.50$	$72.2^{+0.5}_{-0.5}$ <i>c</i>	$0.53^{+0.01}_{-0.01}$	$0.69^{+0.01}_{-0.01}$	J. P. Anderson et al. (2024)
2007X	$54143.90 \pm 2.50$	$112.6^{+0.6}_{-0.6}$ <i>c</i>	$1.03^{+0.00}_{-0.00}$	$1.20^{+0.00}_{-0.00}$	J. P. Anderson et al. (2024)
2008K	$54477.70 \pm 2.00$	$92.6^{+0.8}_{-0.8}$ <i>c</i>	$1.13^{+0.01}_{-0.01}$	$1.31^{+0.00}_{-0.00}$	J. P. Anderson et al. (2024)

Table 3 continued

Table 3 (continued)

SN Name	$t_{\text{exp}}$ [MJD]	$t_{\text{PT}}$ [days]	$(g-r)_{t_{\text{PT}}/2}$ [mag]	$(B-V)_{t_{\text{PT}}/2}$ [mag]	Reference of photometry data
2008bu	$54566.80 \pm 3.50$	$53.7^{+1.0}_{-1.0}{}^c$	$0.47^{+0.01}_{-0.01}$	$0.60^{+0.01}_{-0.01}$	J. P. Anderson et al. (2024)
ASASSN-15bb	57037.50	$107.8^{+17.5}_{-17.5}{}^c$	$0.61^{+0.05}_{-0.10}$	$0.82^{+0.05}_{-0.09}$	J. P. Anderson et al. (2024)
2023axu	$59971.48 \pm 0.01$	$101.2^{+0.3}_{-0.3}$	$0.40^{+0.01}_{-0.01}$	$0.63^{+0.08}_{-0.10}$	M. Shrestha et al. (2024)
2018inm	$58433.41 \pm 0.46$	$75.1^{+1.2}_{-0.9}$	$0.78^{+0.09}_{-0.07}$	–	This work
2019va	$58497.61 \pm 1.51$	$122.1^{+1.4}_{-7.5}$	$0.66^{+0.03}_{-0.11}$	–	This work
2019amt	$58513.93 \pm 0.24$	$128.0^{+3.4}_{-2.4}$	$0.49^{+0.20}_{-0.02}$	–	This work
2019awk	$58524.48 \pm 0.95$	$78.6^{+0.2}_{-0.7}$	$0.51^{+0.18}_{-0.22}$	–	This work
2019cec	$58561.86 \pm 0.23$	$108.0^{+2.3}_{-3.4}$	$0.63^{+0.19}_{-0.03}$	–	This work
2019cct	$58563.29 \pm 0.87$	$104.0^{+0.7}_{-0.1}$	$1.31^{+0.09}_{-0.42}$	–	This work
2019ceg	$58564.87 \pm 1.23$	$124.0^{+1.4}_{-3.6}$	$0.96^{+0.12}_{-0.15}$	–	This work
2019cpo	$58565.29 \pm 1.43$	$125.9^{+0.3}_{-0.6}$	$1.12^{+0.09}_{-0.12}$	–	This work
2019cvz	$58576.46 \pm 0.47$	$118.0^{+5.4}_{-0.5}$	$0.69^{+0.01}_{-0.02}$	–	This work
2019dek	$58577.93 \pm 1.18$	$98.9^{+1.6}_{-1.4}$	$0.92^{+0.18}_{-0.11}$	–	This work
2019fce	$58611.48 \pm 1.95$	$106.6^{+0.2}_{-0.7}$	$0.90^{+0.25}_{-0.19}$	–	This work
2019fem	$58614.42 \pm 0.92$	$95.3^{+0.3}_{-0.5}$	$0.90^{+0.23}_{-0.07}$	–	This work
2019gmh	$58634.28 \pm 0.45$	$120.5^{+9.1}_{-2.6}$	$0.86^{+0.33}_{-0.33}$	–	This work
2019hrb	$58638.93 \pm 0.73$	$103.1^{+7.1}_{-0.8}$	$1.32^{+0.43}_{-0.05}$	–	This work
2019hpb	$58644.96 \pm 0.72$	$105.3^{+2.5}_{-0.3}$	$0.64^{+0.17}_{-0.03}$	–	This work
2019iex	$58660.45 \pm 0.00$	$114.4^{+0.1}_{-0.8}$	$0.66^{+0.03}_{-0.01}$	–	This work
2019lkx	$58676.95 \pm 0.74$	$126.9^{+0.9}_{-0.1}$	$0.55^{+0.07}_{-0.04}$	–	This work
2019mfu	$58691.97 \pm 0.71$	$119.9^{+4.1}_{-0.7}$	$0.93^{+0.09}_{-0.12}$	–	This work
2019nzy	$58711.90 \pm 0.24$	$100.9^{+2.2}_{-2.5}$	$0.37^{+0.03}_{-0.20}$	–	This work
2019odf	$58714.89 \pm 0.25$	$128.1^{+0.9}_{-3.9}$	$0.66^{+0.16}_{-0.02}$	–	This work
2019ovq	$58718.99 \pm 2.21$	$101.9^{+8.5}_{-7.2}$	$0.56^{+0.18}_{-0.16}$	–	This work
2019pkh	$58722.46 \pm 0.49$	$128.4^{+0.2}_{-0.7}$	$0.58^{+0.06}_{-0.09}$	–	This work
2019roa	$58749.50 \pm 0.97$	$107.6^{+0.1}_{-1.7}$	$0.79^{+0.21}_{-0.24}$	–	This work
2019rms	$58752.57 \pm 1.46$	$117.3^{+2.8}_{-0.1}$	$0.75^{+0.04}_{-0.06}$	–	This work
2020gpe	$58947.82 \pm 1.62$	$80.3^{+1.9}_{-1.0}$	$0.73^{+0.08}_{-0.06}$	–	This work
2020jww	$58982.37 \pm 0.51$	$96.2^{+1.7}_{-1.2}$	$0.77^{+0.12}_{-0.13}$	–	This work
2020kdb	$58982.96 \pm 0.74$	$111.0^{+1.2}_{-0.6}$	$0.52^{+0.35}_{-0.05}$	–	This work
2020lfn	$58995.79 \pm 0.23$	$74.4^{+0.2}_{-0.7}$	$0.51^{+0.03}_{-0.04}$	–	This work
2020nqo	$59026.90 \pm 0.76$	$100.7^{+0.4}_{-0.6}$	$0.81^{+0.03}_{-0.07}$	–	This work
2020ovk	$59041.42 \pm 0.46$	$104.0^{+1.7}_{-1.1}$	$0.66^{+0.18}_{-0.07}$	–	This work
2020rhg	$59068.49 \pm 0.98$	$89.4^{+5.1}_{-3.6}$	$0.80^{+0.12}_{-0.13}$	–	This work
2020rka	$59070.45 \pm 0.47$	$75.0^{+3.3}_{-0.5}$	$0.74^{+0.20}_{-0.35}$	–	This work
2020rth	$59075.95 \pm 0.23$	$122.5^{+0.4}_{-1.6}$	$0.87^{+0.08}_{-0.02}$	–	This work
2021cwe	$59256.96 \pm 0.74$	$97.1^{+0.7}_{-1.1}$	$0.26^{+0.08}_{-0.08}$	–	This work
2021ech	$59274.32 \pm 0.42$	$114.7^{+0.1}_{-0.8}$	$1.02^{+0.09}_{-0.08}$	–	This work
2021enz	$59275.85 \pm 0.20$	$108.4^{+1.6}_{-0.4}$	$0.58^{+0.06}_{-0.04}$	–	This work
2021gvv	$59293.97 \pm 0.73$	$98.4^{+2.7}_{-5.9}$	$0.51^{+0.05}_{-0.06}$	–	This work

Table 3 continued

Table 3 (continued)

SN Name	$t_{\text{exp}}$ [MJD]	$t_{\text{PT}}$ [days]	$(g - r)_{t_{\text{PT}}/2}$ [mag]	$(B - V)_{t_{\text{PT}}/2}$ [mag]	Reference of photometry data
2021hse	$59302.92 \pm 0.23$	$100.5^{+1.1}_{-0.8}$	$0.32^{+0.26}_{-0.07}$	–	This work
2021jsf	$59313.95 \pm 1.70$	$96.9^{+1.2}_{-1.7}$	$0.53^{+0.33}_{-0.09}$	–	This work
2021kfo	$59320.42 \pm 0.44$	$99.1^{+0.3}_{-1.7}$	$0.53^{+0.22}_{-0.04}$	–	This work
2021qiu	$59380.92 \pm 0.23$	$114.4^{+0.4}_{-3.4}$	$0.78^{+0.04}_{-0.05}$	–	This work
2022jnh	$59704.86 \pm 1.19$	$115.0^{+6.0}_{-3.6}$	$0.91^{+0.22}_{-0.05}$	–	This work
2022jps	$59704.86 \pm 1.21$	$82.5^{+0.4}_{-1.5}$	$0.54^{+0.36}_{-0.03}$	–	This work
2022jpw	$59705.42 \pm 1.43$	$136.4^{+1.8}_{-0.1}$	$0.86^{+0.24}_{-0.03}$	–	This work
2022kbm	$59713.33 \pm 0.43$	$112.8^{+1.4}_{-12.3}$	$0.71^{+0.07}_{-0.16}$	–	This work
2022knz	$59718.81 \pm 0.22$	$85.7^{+0.5}_{-4.3}$	$0.83^{+0.13}_{-0.08}$	–	This work
2022mxv	$59745.92 \pm 1.22$	$142.0^{+1.6}_{-4.2}$	$0.48^{+0.11}_{-0.01}$	–	This work
2022ojo	$59761.51 \pm 1.44$	$113.9^{+1.2}_{-0.7}$	$1.43^{+0.04}_{-0.04}$	–	This work
2022okz	$59762.00 \pm 0.27$	$81.6^{+1.9}_{-1.0}$	$0.39^{+0.06}_{-0.07}$	–	This work
2022omr	$59766.92 \pm 0.72$	$124.6^{+0.2}_{-1.9}$	$0.71^{+0.08}_{-0.06}$	–	This work
2022ovb	$59773.40 \pm 0.47$	$101.6^{+2.6}_{-0.5}$	$0.71^{+0.02}_{-0.03}$	–	This work
2022rgd	$59803.93 \pm 0.23$	$119.6^{+4.2}_{-0.7}$	$0.92^{+0.27}_{-0.38}$	–	This work
2023eqx	$60037.43 \pm 2.44$	$99.5^{+0.6}_{-1.3}$	$0.51^{+0.07}_{-0.06}$	–	This work
2023eyj	$60037.43 \pm 2.42$	$99.8^{+0.4}_{-3.6}$	$1.01^{+0.27}_{-0.04}$	–	This work
2023iwz	$60079.88 \pm 0.73$	$107.4^{+1.1}_{-7.0}$	$0.94^{+0.08}_{-0.05}$	–	This work
2023ksz	$60101.80 \pm 0.67$	$100.9^{+1.2}_{-0.8}$	$0.83^{+0.15}_{-0.18}$	–	This work
2023kui	$60106.86 \pm 1.13$	$114.4^{+0.9}_{-2.9}$	$0.81^{+0.35}_{-0.27}$	–	This work
2024fcp	$60393.91 \pm 1.18$	$64.0^{+1.1}_{-0.8}$	$0.35^{+0.12}_{-0.08}$	–	This work
2024gvd	$60414.48 \pm 0.93$	$103.4^{+0.6}_{-1.3}$	$0.65^{+0.14}_{-0.11}$	–	This work
2024grw	$60415.81 \pm 0.65$	$83.3^{+1.5}_{-0.5}$	$0.65^{+0.04}_{-0.05}$	–	This work
2024pkt	$60503.99 \pm 0.26$	$120.6^{+0.4}_{-1.5}$	$0.67^{+0.03}_{-0.03}$	–	This work
2024tzc	$60550.41 \pm 0.46$	$111.1^{+1.5}_{-2.3}$	$1.17^{+0.16}_{-0.09}$	–	This work

NOTE— Unless otherwise noted,  $t_{\text{exp}}$  and  $t_{\text{PT}}$  are taken from the photometry reference in the last column.  $(g - r)_{t_{\text{PT}}/2}$  and  $(B - V)_{\text{mid}}$  are derived in this work for all SNe. Superscripts indicate that  $t_{\text{exp}}$  and/or  $t_{\text{PT}}$  are adopted from an alternative source or derived in this work as follows: <sup>a</sup> S. Valenti et al. (2016); <sup>b</sup> C. P. Gutiérrez et al. (2017); <sup>c</sup> J. P. Anderson et al. (2014); <sup>d</sup> This work.

## B. THE INFERRED PROPERTIES FROM LIGHT-CURVE MODELS WITH A THEORETICALLY EXPECTED $M(^{56}\text{Ni})$

The properties of the explosions and progenitors for the ECSN candidates, inferred from the multicolor light curve models with a theoretical  $M(^{56}\text{Ni})$  estimate (S. Wanaajo et al. 2009) are shown in Table 4.

*Facilities:* IRSA

*Software:* STELLA (S. I. Blinnikov & O. S. Bartunov 1993; S. I. Blinnikov et al. 1998; S. Blinnikov et al. 2000),

AstroPy (The Astropy Collaboration et al. 2013, 2018, 2022), NumPy (C. R. Harris et al. 2020), pandas (Wes McKinney 2010; The pandas development team 2025), SciPy (P. Virtanen et al. 2020), Matplotlib (J. D. Hunter 2007; The Matplotlib development team 2025)

## REFERENCES

Anderson, J. P., González-Gaitán, S., Hamuy, M., et al. 2014, ApJ, 786, 67

Anderson, J. P., Contreras, C., Stritzinger, M. D., et al. 2024, A&A, 692, A95

**Table 4.** Properties of the ECSN candidates, inferred from the multicolor light-curve modelings with a theoretically expected  $M(^{56}\text{Ni})$ 

SN Name	$M_{\text{env}}$	$X(\text{H})_{\text{env}}$	$E_{\text{exp}}$	$\dot{M}$	$r_{\text{CSM}}$	$v_0$	$v_\infty$	$\beta$	CSM mass
	$[M_\odot]$		$[10^{50} \text{ ergs}]$	$[M_\odot \text{ yr}^{-1}]$	$[10^{14} \text{ cm}]$	$[\text{km/s}]$	$[\text{km/s}]$		$[M_\odot]$
ASASSN-14ha	4.7	0.7	0.4	$3 \times 10^{-3}$	3	5	10	5	0.04
2018zd	4.7	0.7	0.6	$10^{-2}$	6	5	10	5	0.27
2023axu	4.7	0.5	1.4	$10^{-2}$	10	5	10	4	0.39
2019amt	4.7	0.7	0.9	$10^{-2}$	30	1	10	5	1.64
2019lkx	4.7	0.7	1.0	$10^{-2}$	30	5	10	1	0.99
2019nzy	3.0	0.7	1.0	$10^{-2}$	30	5	10	1	1.00
2019pkh	4.7	0.5	0.5	$10^{-2}$	10	5	10	3	0.37
2021cwe	4.7	0.5	1.4	$10^{-2}$	10	5	10	4	0.39
2021hse	4.7	0.5	1.3	$10^{-2}$	10	5	10	3	0.37
2022mxv	4.7	0.7	2.7	$10^{-2}$	30	5	10	5	1.14

- Arnett, W. D. 1980, ApJ, 237, 541
- Bellm, E. C., Kulkarni, S. R., Graham, M. J., et al. 2018, PASP, 131, 018002
- Bessell, M. S. 2005, ARA&A, 43, 293
- Bethe, H. A. 1985, ApJ, 295, 14
- Blinnikov, S., Lundqvist, P., Bartunov, O., Nomoto, K., & Iwamoto, K. 2000, ApJ, 532, 1132
- Blinnikov, S. I., & Bartunov, O. S. 1993, A&A, 273, 106
- Blinnikov, S. I., Eastman, R., Bartunov, O. S., Popolitov, V. A., & Woosley, S. E. 1998, ApJ, 496, 454
- Bruch, R. J., Gal-Yam, A., Schulze, S., et al. 2021, ApJ, 912, 46
- Bruch, R. J., Gal-Yam, A., Yaron, O., et al. 2023, ApJ, 952, 119
- Chevalier, R. A., & Irwin, C. M. 2011, ApJL, 729, L6
- Colgate, S. A., & White, R. H. 1966, ApJ, 143, 626
- Cook, D. O., Kasliwal, M. M., Van Sistine, A., et al. 2019, ApJ, 880, 7
- Das, K. K., Kasliwal, M. M., Fremling, C., et al. 2025a, PASP, 137, 044203
- Das, K. K., Kasliwal, M. M., Sollerman, J., et al. 2025b, arXiv [astro-ph.HE]
- Davidson, K., Gull, T. R., Maran, S. P., et al. 1982, ApJ, 253, 696
- De, K., Kasliwal, M. M., Tzanidakis, A., et al. 2020, ApJ, 905, 58
- de Jaeger, T., Anderson, J. P., Galbany, L., et al. 2018, MNRAS, 476, 4592
- Dessart, L., & Hillier, D. J. 2005, A&A, 439, 671
- Doherty, C. L., Gil-Pons, P., Siess, L., & Lattanzio, J. C. 2017, PASA, 34
- Eastman, R. G., & Kirshner, R. P. 1989, ApJ, 347, 771
- Eastman, R. G., Woosley, S. E., Weaver, T. A., et al. 1994, ApJ
- Faran, T., Poznanski, D., Filippenko, A. V., et al. 2014, MNRAS, 442, 844
- Felipe, O. E., Hamuy, M., Pignata, G., et al. 2010, ApJ, 715, 833
- Fukugita, M., Ichikawa, T., Gunn, J. E., et al. 1996, AJ, 111, 1748
- Förster, F., Cabrera-Vives, G., Castillo-Navarrete, E., et al. 2021, AJ, 161, 242
- Galbany, L., Hamuy, M., Phillips, M. M., et al. 2016, AJS, 151, 33
- Gutiérrez, C. P., Anderson, J. P., Hamuy, M., et al. 2017, ApJ, 850, 89
- Harris, C. R., Millman, K. J., van der Walt, S. J., et al. 2020, Nature, 585, 357
- Hiramatsu, D., Berger, E., Gomez, S., et al. 2024, arXiv [astro-ph.HE], arXiv:2411.07287
- Hiramatsu, D., Howell, D. A., Van Dyk, S. D., et al. 2021, NatAs, 5, 903
- Hunter, J. D. 2007, Computing in Science & Engineering, 9, 90
- Janka, H.-T., Müller, B., Kitaura, F. S., & Buras, R. 2008, A&A, 485, 199
- Kasen, D., Branch, D., Baron, E., & Jeffery, D. 2001, arXiv [astro-ph]
- Kasen, D., & Woosley, S. E. 2009, ApJ, 703, 2205
- Kitaura, F. S., Janka, H.-T., & Hillebrandt, W. 2006, A&A, 450, 345
- Komatsu, E., Smith, K. M., Dunkley, J., et al. 2011, ApJS, 192, 18

- Kozyreva, A., Baklanov, P., Jones, S., Stockinger, G., & Janka, H.-T. 2021, *MNRAS*, 503, 797
- Kozyreva, A., Nakar, E., & Waldman, R. 2019, *MNRAS*, 483, 1211
- Langer, N. 2012, *ARA&A*, 50, 107
- Leaman, J., Li, W., Chornock, R., & Filippenko, A. V. 2011, *MNRAS*, 412, 1419
- Leonard, D. C., Filippenko, A. V., Li, W., et al. 2002, *Astron. J.*, 124, 2490
- Li, W., Chornock, R., Leaman, J., et al. 2011a, *MNRAS*, 412, 1473
- Li, W., Leaman, J., Chornock, R., et al. 2011b, *MNRAS*, 412, 1441
- Limongi, M., Roberti, L., Chieffi, A., & Nomoto, K. 2024, *ApJS*, 270, 29
- Litvinova, I. Y., & Nadezhin, D. K. 1985, *SvAL*, 11, 351
- LSST Science Collaboration, Abell, P. A., Allison, J., et al. 2009, *arXiv [astro-ph.IM]*, [arXiv:0912.0201](https://arxiv.org/abs/0912.0201)
- Martínez, L., Bersten, M. C., Anderson, J. P., et al. 2022, *A&A*, 660, A41
- Masci, F. J., Laher, R. R., Rusholme, B., et al. 2019, *PASP*, 131, 018003
- Miyaji, S., Nomoto, K., Koichi, Y., & Sugimoto, D. 1980, *PASJ*, 32, 303
- Moriya, T., Tominaga, N., Blinnikov, S. I., Baklanov, P. V., & Sorokina, E. I. 2011, *MNRAS*, 415, 199
- Moriya, T. J., Förster, F., Yoon, S.-C., Gräfener, G., & Blinnikov, S. I. 2018, *MNRAS*, 476, 2840
- Moriya, T. J., Pruzhinskaya, M. V., Ergon, M., & Blinnikov, S. I. 2015, *MNRAS*, 455, 423
- Moriya, T. J., Tominaga, N., Langer, N., et al. 2014, *A&A*, 569, A57
- Morozova, V., Piro, A. L., & Valenti, S. 2017, *ApJ*, 838, 28
- Nadyozhin, D. K. 1994, *ApJS*, 92, 527
- Nakar, E., Poznanski, D., & Katz, B. 2016, *ApJ*, 823, 127
- Nomoto, K. 1984, *ApJ*, 277, 791
- Nomoto, K. 1987, *ApJ*, 322, 206
- Nomoto, K., Sparks, W. M., Fesen, R. A., et al. 1982, *Nature*, 299, 803
- Pastorello, A., Zampieri, L., Turatto, M., et al. 2004, *MNRAS*, 347, 74
- Pastorello, A., Valenti, S., Zampieri, L., et al. 2009, *MNRAS*, 394, 2266
- Pessi, T., Desai, D. D., Prieto, J. L., et al. 2025, *arXiv [astro-ph.HE]*
- Poelarends, A. J. T., Herwig, F., Langer, N., & Heger, A. 2008, *ApJ*, 675, 614
- Poole, T. S., Breeveld, A. A., Page, M. J., et al. 2007, *MNRAS*, 383, 627
- Popov, D. V. 1993, *ApJ*, 414, 712
- Rodríguez, Ó. 2022, *MNRAS*, 515, 897
- Salpeter, E. E. 1955, *ApJ*, 121, 161
- Sato, M., Tominaga, N., Blinnikov, S. I., et al. 2024, *ApJ*, 970, 163
- Schlegel, D. J., Finkbeiner, D. P., & Davis, M. 1998, *ApJ*, 500, 525
- Schmidt, M. 1968, *ApJ*, 151, 393
- Shigeyama, T., & Nomoto, K. 1990, *ApJ*, 360, 242
- Shrestha, M., Pearson, J., Wyatt, S., et al. 2024, *ApJ*, 961, 247
- Shrestha, M., DeSoto, S., Sand, D. J., et al. 2025, *ApJL*, 982, L32
- Siess, L. 2007, *A&A*, 476, 893
- Silva-Farfán, J., Förster, F., Moriya, T. J., et al. 2024, *arXiv*, [arXiv:2404.12620](https://arxiv.org/abs/2404.12620)
- Singh, A., Teja, R. S., Moriya, T. J., et al. 2024, *ApJ*, 975, 132
- Smith, N., Pearson, J., Sand, D. J., et al. 2023, *ApJ*, 956, 46
- Smith, N., Silverman, J. M., Chornock, R., et al. 2009, *ApJ*, 695, 1334
- Spiro, S., Pastorello, A., Pumo, M. L., et al. 2014, *MNRAS*, 439, 2873
- Stockinger, G., Janka, H.-T., Kresse, D., et al. 2020, *MNRAS*, 496, 2039
- Stritzinger, M., Taddia, F., Fransson, C., et al. 2012, *Astrophys. J.*, 756, 173
- Subrayan, B. M., Milisavljevic, D., Moriya, T. J., et al. 2023, *ApJ*, 945, 46
- Sukhbold, T., Ertl, T., Woosley, S. E., Brown, J. M., & Janka, H.-T. 2016, *ApJ*, 821, 38
- Sánchez-Sáez, P., Reyes, I., Valenzuela, C., et al. 2021, *AJ*, 161, 141
- Takiwaki, T., Kotake, K., & Suwa, Y. 2012, *ApJ*, 749, 98
- Tanaka, M., Tominaga, N., Morokuma, T., et al. 2016, *ApJ*, 819, 5
- Temim, T., Laming, J. M., Kavanagh, P. J., et al. 2024, *ApJL*, 968, L18
- The Astropy Collaboration, Robitaille, T. P., Tollerud, E. J., et al. 2013, *Astron. Astrophys.*, 558, A33
- The Astropy Collaboration, Price-Whelan, A. M., Sipőcz, B. M., et al. 2018, *Astron. J.*, 156, 123
- The Astropy Collaboration, Price-Whelan, A. M., Lim, P. L., et al. 2022, *Astrophys. J.*, 935, 167
- The Matplotlib development team. 2025, *Matplotlib*, 3.10.6 Zenodo
- The pandas development team. 2025, *pandas-dev/pandas: Pandas, v2.3.3 Zenodo*
- Tominaga, N., Blinnikov, S. I., & Nomoto, K. 2013, *ApJL*, 771, L12

- Tominaga, N., Morokuma, T., Tanaka, M., et al. 2019, *ApJ*, 885, 13
- Toshikage, S., Tanaka, M., Yasuda, N., et al. 2024, *ApJ*, 977, 18
- Utrobin, V. P., & Chugai, N. N. 2005, *A&A*, 441, 271
- Valenti, S., Benetti, S., Cappellaro, E., et al. 2007, *MNRAS*, 383, 1485
- Valenti, S., Howell, D. A., Stritzinger, M. D., et al. 2016, *MNRAS*, 459, 3939
- Valerin, G., Pumo, M. L., Pastorello, A., et al. 2022, *MNRAS*, 513, 4983
- Van Dyk, S. D., de Graw, A., Baer-Way, R., et al. 2022, *MNRAS*, 519, 471
- Virtanen, P., Gommers, R., Oliphant, T. E., et al. 2020, *Nature Methods*, 17, 261
- Wanajo, S., Müller, B., Janka, H.-T., & Heger, A. 2018, *ApJ*, 852, 40
- Wanajo, S., Nomoto, K., Janka, H.-T., Kitaura, F. S., & Müller, B. 2009, *ApJ*, 695, 208
- Wes McKinney. 2010, in *Proceedings of the 9th Python in Science Conference*, ed. Stéfan van der Walt & Jarrod Millman, 56–61
- Woodsley, S. E., Heger, A., & Weaver, T. A. 2002, *RvMP*, 74, 1015
- Yaron, O., & Gal-Yam, A. 2012, *PASP*, 124, 668
- Yaron, O., Perley, D. A., Gal-Yam, A., et al. 2017, *NatPh*, 13, 510
- Zhang, J., Wang, X., József, V., et al. 2020, *MNRAS*, 498, 84